A&A, 706, A81 (2026)
https://doi.org/10.1051/0004-6361/202558091
© The Authors 2026

Astronomy & Astrophysics

SDSS-V LVM: Resolving physical conditions in the Trifid Nebula

Natascha Sattler[1,⋆], J. Eduardo Méndez-Delgado[1,2], Kathryn Kreckel[1], Christophe Morisset[3,4], Oleg Egorov[1], Evgeniya Egorova[1], Ahmad Nemer[5,6], Fu-Heng Liang[1], A. A. C. Sander[1,7], Alexandre Roman-Lopes[8], Carlos G. Román-Zúñiga[3], Evelyn J. Johnston[9], Sebastián F. Sánchez[3,10], José G. Fernández-Trincado[11], Niv Drory[12], Amrita Singh[13], Dmitry Bizyaev[14], Sumit K. Sarbadhicary[15,16,17], Pablo García[18,19], Alfredo Mejía-Narváez[20], and Guillermo A. Blanc[13,21]

[1] Astronomisches Rechen-Institut, Zentrum für Astronomie der Universität Heidelberg, Mönchhofstraße 12-14, 69120 Heidelberg, Germany
[2] Instituto de Astronomía, Universidad Nacional Autónoma de México, Ap. 70-264, 04510 CDMX, Mexico
[3] Instituto de Astronomía, Universidad Nacional Autónoma de México, Ap. 106, 22800 Ensenada, BC, Mexico
[4] Instituto de Ciencias Físicas, Universidad Nacional Autónoma de México, Av. Universidad s/n, 62210 Cuernavaca, Morelos, Mexico
[5] New York University Abu Dhabi, PO Box 129188, Abu Dhabi, UAE
[6] Center for Astrophysics and Space Science, NYU Abu Dhabi, PO Box 129188, Abu Dhabi, UAE
[7] Universität Heidelberg, Interdisziplinäres Zentrum für Wissenschaftliches Rechnen, 69120 Heidelberg, Germany
[8] Department of Astronomy / Departamento de Astronomía, Universidad de La Serena, La Serena, Chile
[9] Instituto de Estudios Astrofísicos, Facultad de Ingeniería y Ciencias, Universidad Diego Portales, Av. Ejército Libertador 441, Santiago, Chile
[10] Instituto de Astrofísica de Canarias, La Laguna, Tenerife, 38200 Spain
[11] Universidad Católica del Norte, Núcleo UCN en Arqueología Galáctica - Inst. de Astronomía, Av. Angamos 0610, Antofagasta, Chile
[12] McDonald Observatory, The University of Texas at Austin, 1 University Station, Austin, TX 78712-0259, USA
[13] Departamento de Astronomía, Universidad de Chile, Camino del Observatorio 1515, Las Condes, Santiago, Chile
[14] Apache Point Observatory and New Mexico State University, PO Box 59, Sunspot, NM, 88349-0059, USA
[15] Department of Physics and Astronomy, The Johns Hopkins University, Baltimore, MD 21218, USA
[16] Department of Physics, The Ohio State University, Columbus, Ohio 43210, USA
[17] Center for Cosmology & Astro-Particle Physics, The Ohio State University, Columbus, Ohio 43210, USA
[18] Chinese Academy of Sciences South America Center for Astronomy, National Astronomical Observatories, CAS, Beijing 100101, China
[19] Instituto de Astronomía, Universidad Católica del Norte, Av. Angamos 0610, Antofagasta, Chile
[20] Universidad de Chile, Av. Libertador Bernardo O'Higgins 1058, Santiago, Chile
[21] Observatories of the Carnegie Institution for Science, 813 Santa Barbara Street, Pasadena, CA 91101, USA

Received 13 November 2025 / Accepted 2 December 2025

ABSTRACT

Aims. The chemical abundance of the interstellar medium sets the initial conditions for star formation and provides a probe of chemical galaxy evolution models. However, unresolved inhomogeneities in the electron temperature can lead to a systematic underestimation of the abundances. We aim to directly test this effect.

Methods. We used the SDSS-V Local Volume Mapper to spatially map the physical conditions of the Trifid Nebula (M 20), a Galactic H II region ionized by a single mid-type O-star, at a 0.24 pc resolution. We exploited various emission lines (e.g., Hydrogen recombination lines and collisionally excited lines, including also faint auroral lines) and computed the spatially resolved maps of [O II] and [S II] electron densities, the [N II], [O II], [S II], and [S III] electron temperatures, and the ionic oxygen abundances.

Results. We found internal variations of electron density that result from the ionization front, along with a negative radial gradient. However, we did not find any strong gradients or structures in the electron temperature and the total oxygen abundance, making the Trifid Nebula a relatively homogeneous H II region at the observed spatial scale. We compared these spatially resolved properties with equivalent integrated measurements of the Trifid Nebula and found no significant variations between integrated and spatially resolved conditions.

Conclusions. This isolated H II region, ionized by a single O-star, represents a test case of an ideal Strömgren sphere. The physical conditions in the Trifid Nebula behave as expected, with no significant differences between integrated and resolved measurements.

Key words. ISM: abundances – ISM: general – HII regions – ISM: structure – local insterstellar matter – ISM: individual objects: M 20

⋆ Corresponding author: nataschasattler@outlook.de

Open Access article, published by EDP Sciences, under the terms of the Creative Commons Attribution License (https://creativecommons.org/licenses/by/4.0), which permits unrestricted use, distribution, and reproduction in any medium, provided the original work is properly cited.
This article is published in open access under the Subscribe to Open model. Subscribe to A&A to support open access publication.

1. Introduction

During the process of galaxy evolution, gas from the interstellar medium (ISM) is enriched by stellar feedback from the current generation of stars, through supernovae explosions and stellar winds (e.g., Gallart et al. 2019; Martig et al. 2021; Conroy et al. 2022). This enriched gas mixes into the ISM of the galaxy and eventually forms a new generation of stars with higher metal abundances (e.g., Worthey et al. 1992; Mo et al. 2010; Peletier 2013). Therefore, to understand galaxy formation and test models of chemical galaxy evolution, we need to determine the current elemental abundances, as they contain a record of the galaxy's formation history (e.g., Peimbert et al. 2017; Maiolino & Mannucci 2019). This can be achieved by measuring the current chemical gas-phase abundances of star-forming H II regions via bright optical emission lines (e.g., Pérez-Montero 2017; Peimbert et al. 2017; Kewley et al. 2019b). H II regions are primarily composed of hydrogen ionized by young massive stars (e.g., O-type stars) with a high rate of hydrogen-ionizing photon emission. In addition, these regions also contain helium and heavier elements such as oxygen, nitrogen, and sulfur (e.g., Esteban et al. 2017, 2025).

The temperature of the gas in the H II region is governed by a balance of heating and cooling processes. The ISM gas is mainly heated by photoionization from the stellar ionizing sources, then cooled through recombination, free-free radiation, and collisionally excited line (CEL) radiation (Osterbrock & Ferland 2006; Peimbert et al. 2017). The free-free cooling is dominated by the hydrogen ions, due to their abundance in the ISM. On the other hand, heavier ions such as oxygen or nitrogen contribute significantly to the cooling via CEL radiation because they have low-lying energy levels that are similar in energy to the kinetic energy of free electrons. This allows these heavier ions to be easily excited through collisions, whereas hydrogen and helium have much higher excitation potentials. Therefore, each element contributes to a different cooling mechanism, which makes the equilibrium temperature of the gas in the H II region strongly dependent on the abundances of the different elements.

During these cooling processes, various kinds of emission lines are produced in the nebula. The recombination cooling is responsible for the observed recombination lines (RL) that are primarily produced by hydrogen, giving rise to the Balmer, Paschen, and other hydrogen emission series. Cooling through collisionally excited lines (CEL) in the optical mostly occurs via transitions that are forbidden in the electric dipole approximation but can proceed through less probable magnetic dipole (M1) or electric quadrupole (E2) mechanisms. Well-known examples include the strong [O III]λ5007 (M1) line and the weaker [O III]λ4931 (E2) line. The very low densities in ionized nebulae prevent collisional de-excitation, allowing these forbidden lines to become efficient cooling channels (Baker et al. 1938). The relative fluxes of different emission lines are sensitive to the electron density, electron temperature, and the ionic abundances, hence can be used as a diagnostic of the H II region's physical conditions (Osterbrock & Ferland 2006; Draine 2011).

It is often assumed that H II regions are homogeneous systems (e.g., Filippenko 1985; Osterbrock 1989); however, the density and temperature distributions across observed H II regions are not uniform, and spatial variations or inhomogeneities are measured (e.g., Copetti et al. 2000; Malmann et al. 2002). Most H II regions show filamentary or shell-like electron density structures (e.g., Kennicutt 1984) and show a variety of radial gradients in density (e.g., Binette et al. 2002; Herrera-Camus et al. 2016; Rubin et al. 2016). Similarly, the electron temperature also shows inhomogeneities that have been theorized to cause underestimations of the ionic abundances (e.g., Peimbert et al. 2004; Hägele et al. 2006; Peimbert et al. 2017; Kewley et al. 2019a). However, measuring the electron temperature and its variations is challenging, as the measurements rely on faint auroral lines that are difficult to detect (e.g., Hägele et al. 2006; Kewley et al. 2019b). These variations may come from shock waves and turbulence (Peimbert et al. 1991; O'Dell et al. 2015; Arthur et al. 2016; Royer et al. 2025), stellar winds from planetary nebula (Peimbert et al. 1995) or Wolf-Rayet stars (Gonzalez-Delgado et al. 1994), and inhomogeneities in density or the distribution of multiple ionization sources (Arthur & Hoare 2006; O'Dell et al. 2017). Controversially, some studies have reported no evidence of temperature fluctuations in single nebula (e.g., Liu et al. 2006; Stasińska et al. 2013).

Internal variations of electron density and temperature may affect the calculation of the intrinsic ionic abundances, as temperature inhomogeneities are known to lead to an underestimation in the calculation of abundances, if not properly taken into account (Peimbert et al. 2017; Méndez-Delgado et al. 2022a, 2023a,b). In particular, in integrated extra-galactic H II regions or long-slit observations, the temperature inhomogeneities cannot be resolved and need to be estimated by comparing different ionic temperature measurements. This is because ions with different ionization potentials dominate in distinct regions of the nebula, so their temperatures probe different physical zones (Peimbert et al. 2017). Since abundance determinations depend on these ionic temperatures, unresolved observations can introduce systematic biases in the derived ionic abundances. Therefore, we need spatially resolved observations of H II regions to directly measure the extent of density and temperature inhomogeneities and obtain more accurate abundances.

Previous approaches using integral field unit (IFU) data to study the detailed structures of H II regions have been reported in the literature (Sánchez et al. 2007; García-Benito et al. 2010; Relaño et al. 2010; López-Hernández et al. 2013; Kumari et al. 2017; Dopita et al. 2019; Jin et al. 2023; Garner et al. 2025; Royer et al. 2025). For four H II regions in the Large and Small Magellanic Clouds at a sampling of around 0.24–0.3 pc, Jin et al. (2023) found negative radial gradients in electron density as well as positive and negative radial gradients in electron temperature. However, the gradients in electron temperature are smaller than the uncertainties, so the measured temperatures across the four nebulae are consistent with being flat. Moreover, Royer et al. (2025) found complex patterns of electronic density and temperature variations across the H II region Sh2-158.

It is possible to achieve a homogeneous spatial sampling of multiple H II regions and the ISM across the local galactic environment with high-quality spectra using the Sloan Digital Sky Survey-V (SDSS-V) Local Volume Mapper (LVM), a recently commissioned spectroscopic survey (Perruchot et al. 2018; Kollmeier et al. 2019; Drory et al. 2024; Blanc et al. 2024; Herbst et al. 2024; Kollmeier et al. 2025). The study by Kreckel et al. (2024) demonstrated the great potential of this survey in their first analysis of a larger region in the Orion nebula.

The Trifid Nebula (M 20), shown in Fig. 1 based on an NSF–DOE Vera C. Rubin Observatory image[1], is a small and nearly symmetrical H II region ionized by HD 164492A, classified as an O 7.5 V star (Sota et al. 2014). However, its measured effective temperature of 38 000 K (Martins et al. 2015) suggests a slightly earlier type, around O 6.5 V. With the ionization dominated by this single O-type star, M 20 offers an ideal laboratory

[1] https://rubinobservatory.org/news/first-imagery-rubin

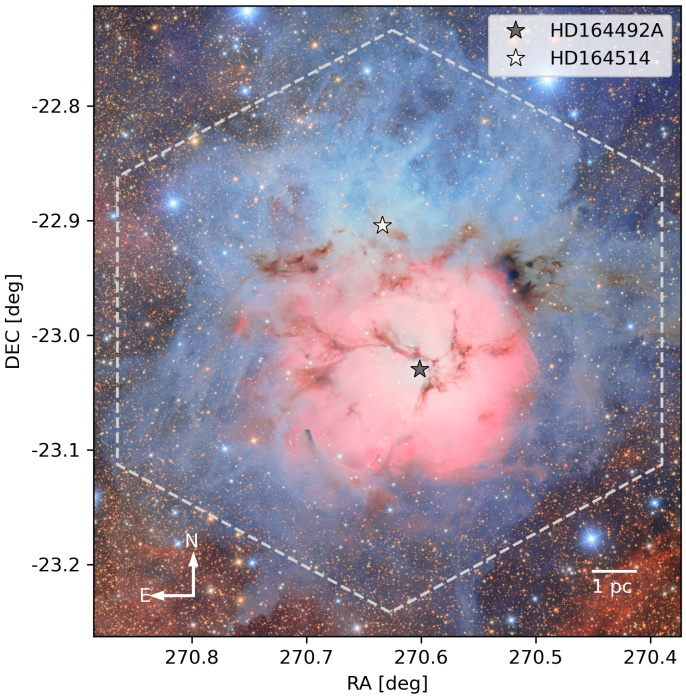

Fig. 1. NSF–DOE Vera C. Rubin Observatory image of the Trifid Nebula, using LSST's (Legacy Survey of Space and Time, Ivezić et al. 2019) six filters: *u*, *g*, *r*, *i*, *z*, and *y*. It shows the glowing pink emission nebula and the cool blue reflection nebula. The position of the central ionizing source HD 164492A is marked with a grey star. The center of Trifid's reflection nebula (Lynds & Oneil 1986) is marked by the A 7 supergiant HD 164514 (white star). The extent of the hexagonal LVM pointing is indicated by a grey dashed line.

for studying spherical symmetry within an individual Strömgren sphere (Strömgren 1939).

HD 164492A exhibits a soft and variable X-ray emission spectrum with $kT \approx 0.5$ keV and $\log L_X/L_{bol} < -7$, likely produced by wind-intrinsic shocks (Rho et al. 2004). This system was investigated for signs of binarity by Stickland & Lloyd (2001), but they could not determine any conclusive insights. While we cannot rule out that HD 164492A is a binary, the available IUE UV spectrum does not show obvious signs of a significantly hotter or cooler companion. A more thorough investigation would be needed to set stronger constraints on multiplicity, although we do not expect that this would lead to a drastically different result in the ionizing photon budget. In addition to the central ionizing star, younger, lower-mass stellar populations (<1 Myr) are present in M 20 (Tapia et al. 2018) along with several protostars (Rho et al. 2001, 2006; Yusef-Zadeh et al. 2005), indicating ongoing star formation.

In this study, we adopted a distance to M 20 of $1.42\ ^{+0.09}_{-0.08}$ kpc calculated by Méndez-Delgado et al. (2022b) using *Gaia* EDR3 parallaxes (Gaia Collaboration 2020) of the central stellar system HD 164492, containing HD 164492A. A reflection nebula, caused by scattered light from the A 7 super-giant HD 164514 (Lynds & Oneil 1986) with a *Gaia* EDR3 distance of 1.191 ± 0.047 kpc (Gaia Collaboration 2020), is located north of the Trifid Nebula. Lynds & Oneil (1986) suggested that the grains in the reflection nebula have a higher albedo than the particles in the Trifid Nebula itself, implying that the O-star HD 164492A must have modified the nature of the surrounding grains.

The current generation of stars in M 20 likely formed about 1 Myr ago following a collision between two molecular clouds (Torii et al. 2011, 2017; Fukui et al. 2021; Kalari 2021), where the ionizing O-type star HD 164492A presumably formed around 0.3 Myr ago (Torii et al. 2017). However, other studies by Fukuda & Hanawa (2000); Rho et al. (2008); Kuhn et al. (2022) suggested that the kinematic features of the clouds may not necessarily come from a cloud-cloud collision but can also be interpreted as the expansion of the H II region or turbulence.

In this paper, we used integral field spectroscopic data from the LVM to spatially map the physical conditions of the Trifid Nebula at 0.24 pc resolution. We organize this paper as follows. First, we describe the observations as well as the data reduction in Sect. 2. Next, we describe the analysis methods to infer physical properties in Sect. 3. Then, we present our results of the electron density, temperature, and ionic abundances in Sect. 4. Further, the results are discussed in Sect. 5 and our conclusions are given in Sect. 6.

2. Observations and data reduction

M 20 was observed as part of the SDSS-V (Kollmeier et al. 2019, 2025) using the LVM, which hosts a stable wide field integral field unit to survey the ionized gas in the Milky Way, Magellanic clouds, and other Local Group galaxies (Drory et al. 2024). The LVM is located at the Las Campanas Observatory in Chile's Atacama Desert and consists of four 16 cm telescopes, each equipped with a fiber bundle (each fiber has a diameter of 35.3 arcsec) that is fed into three DESI spectrographs with R ~ 4000 across 3600–9800 Å (Perruchot et al. 2018; Konidaris et al. 2020; Herbst et al. 2024). This configuration allows us to detect many faint auroral lines, which are important for the measurements of physical conditions. One of those four telescopes, hosting 1801 fibers with a total fill factor of 83%, is used for the observation of the science targets, while the other three telescopes simultaneously observe spectrophotometric stars and sky fields, which are later used in the data reduction. With this setup, one pointing of LVM covers a hexagon of 0.5° diameter, enabling us to observe M 20 within only one LVM pointing, an angular resolution of 35.3 arcsec, and, in particular, a spatial resolution of 0.24 pc. An overview of the full observing strategy will be given in Johnston (in prep.).

In this study, we used eight single-exposure (not dithered) early LVM science frames (taken during September 27–30, 2023), each with an integration time of 15 minutes, leading to a total of 2 hours and therefore a higher signal-to-noise ratio (S/N) than a single frame in LVM's survey mode. The frames are reduced using version 1.1.1 of the dedicated LVM Data Reduction Pipeline (DRP) (Mejia-Narvaez in prep.), which removes instrumental features and sky emission, while calibrating the flux using individual stars in the science field. Then, the eight reduced frames are combined into a single file. This combination of spectra from multiple exposures was done by collecting the single fiber spectra, applying heliocentric velocity corrections, and merging spectra from fibers with matching positions using ASTROPY *sigma_clip* (with $\sigma = 2$) into a mean spectrum for each fiber. The output single frame includes all key spectral extensions (e.g., flux and flux error) and a unified fiber position table for analysis. In this way, we reached a mean 3σ Hα sensitivity of around 6×10^{-16} erg/s/cm^2/arcsec^2 for the full frame. A spectrum of the integrated LVM frame can be seen in Fig. 2, together with a collection of zoom-in views of strong lines and weak auroral lines.

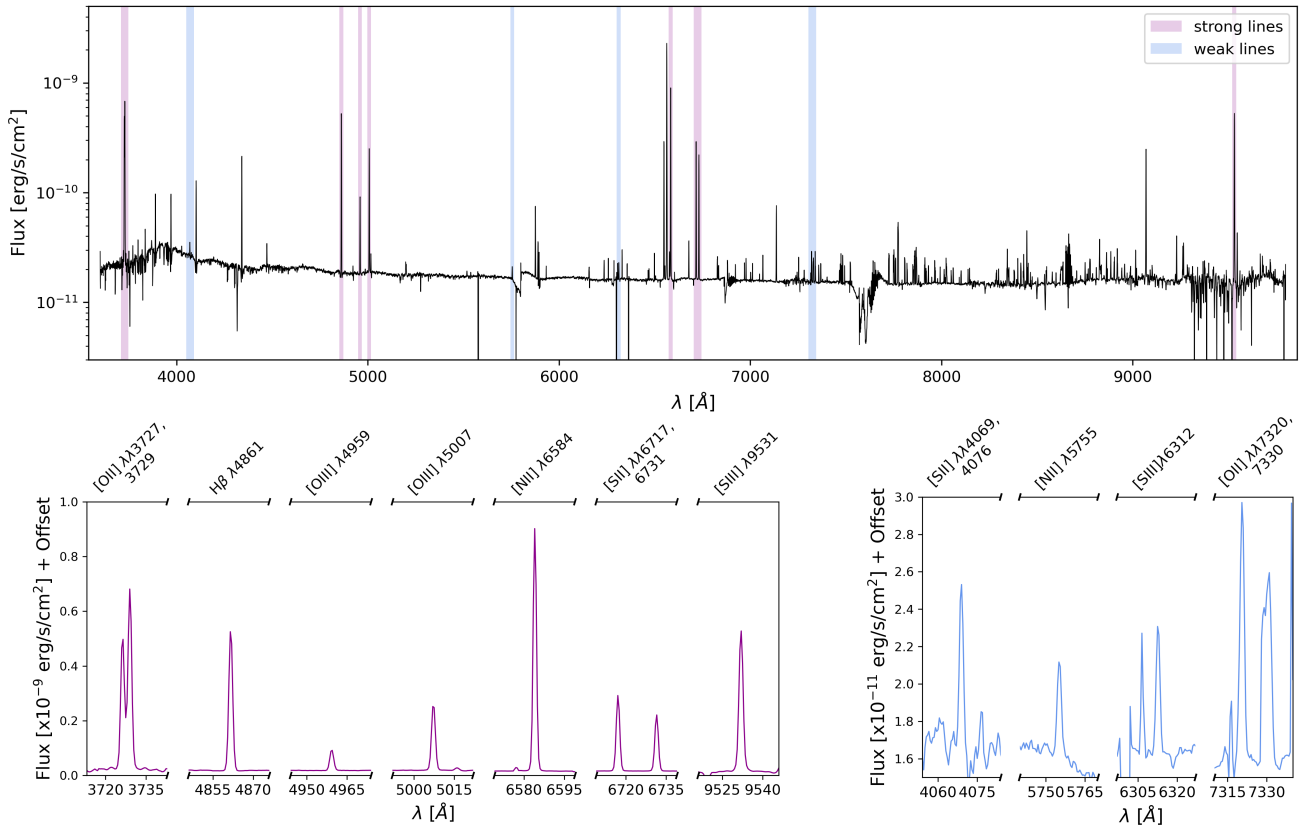

Fig. 2. *Top*: integrated spectrum of the full LVM pointing covering the Trifid Nebula. *Bottom*: zoom-in collection of strong lines (left: in magenta) and weak auroral lines (right: in blue) taken from the above spectrum, each in a window of 30 Å. The Hα emission line is not shown here, as its height would dominate over all other lines.

For each fiber, we fit the emission lines (Hydrogen recombination lines and collisionally excited lines, including faint auroral lines, [O II]$\lambda\lambda$3727,29; [S II]λ4069; [O III]λ5007; [N II]λ5755; [S III]λ6312; [N II]λ6584; [S II]$\lambda\lambda$6717,31; [O II]λ7320, [O II]λ7330; [S III]λ9531), and the continuum spectrum independently and simultaneously. To do so, we used Gaussian profiles for the former and a linear profile for the latter. This nearly linear continuum emission arises primarily from hydrogen free–free and free–bound emission and is removed from the line fits. The [O II]$\lambda\lambda$3727,29 doublet was fitted using a double Gaussian profile, deblending the two emission lines.

To ensure good fits, all spaxels with S/N < 3 in the used diagnostic emission line and errors larger than the measured value itself were masked from the resulting maps (see Sect. 4). Bright stars are negligible in the nebular spectra, as the large field of view of each LVM fiber means that individual stars contribute only to a small fraction of the total light collected and, thus, they do not dominate the signal in their corresponding fibers.

We note that our emission line measurements account for all known limitations of the current DRP version, such as sky subtraction, flat field correction, and flux calibration, since most of the selected emission lines, except Heλ7281 and [S II]λ4069, are not affected by the sky subtraction, and the qualitative comparison of nearby emission lines would not be distorted with other calibrations. Nevertheless, using a future version of the DRP might slightly change the absolute values of electron density, temperature, and ionic abundances by a few percent, but the measured gradients would be expected to remain unaffected.

3. Analysis

3.1. Reddening correction

We applied a reddening correction to the measured fluxes of all spaxels to account for extinction. To do this, we use PYNEB v.1.1.19b2 (Luridiana et al. 2015; Morisset et al. 2020) (together with the atomic data set used in Méndez-Delgado et al. 2025) which follows the well-known relationship,

$$\mathrm{c}\,(\mathrm{H}\beta) = \frac{1}{f\,(\lambda)} \log\left(\frac{\frac{I(\lambda)}{I(\mathrm{H}\beta)}}{\frac{F(\lambda)}{F(\mathrm{H}\beta)}}\right), \quad (1)$$

where c(Hβ) is the reddening coefficient, $f\,(\lambda)$ is the reddening law normalized to Hβ, $I\,(\lambda)$ is the theoretical flux, and $F\,(\lambda)$ is the observed (uncorrected) flux.

To calculate the reddening correction factor c(Hβ) for our H II region, we compared the measured ratios of hydrogen Balmer and Paschen lines with the theoretical values provided by Storey & Hummer (1995) at an electron temperature of 10 000 K and electron density of 100 cm^{-3}. Using other reasonable temperature or density combinations (e.g., the ones calculated in this paper) does not significantly affect the reddening correction factor or the final results and conclusions. We used the reddening law of Cardelli et al. (1989) modified by Blagrave et al. (2007) together with an R_V = 5.5, as measured by Greve (2010) and Cambrésy et al. (2011).

Using PYNEB, the reddening correction factor of each ratio is then extracted with the *cHbeta* function. To get a robust measure, we adopted the median of all calculated correction

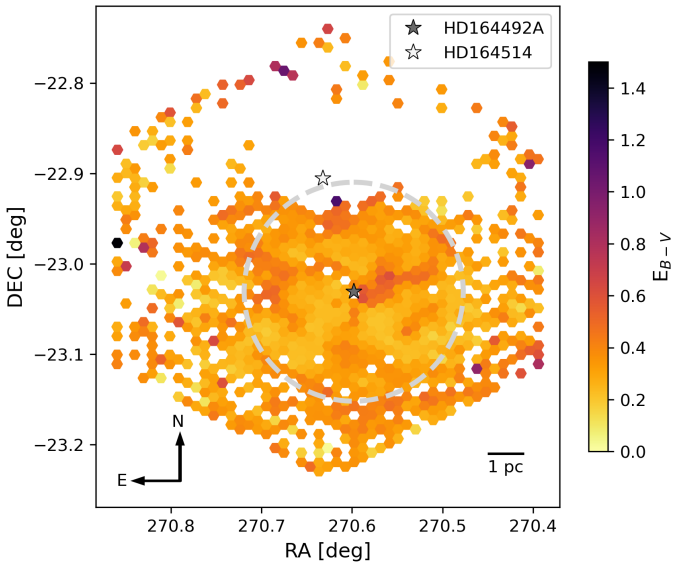

Fig. 3. Spatial map of the dust extinction in M 20. The position of HD 164492A is marked with a grey star. The extent of the measured Strömgren sphere (Sect. 3.4) is shown by a grey dashed circle. The white regions arise from the limited sensitivity to the faint hydrogen emission lines in these spaxels and were masked (see Sect. 2). A uncertainty map is shown in Fig. D.1.

factors derived from the various hydrogen line ratios as our final value of c(Hβ). Here, we make sure to only use hydrogen line ratios that are well measured and yield consistent correction factors (Hλ3771/Hλ6563, Hλ3750/Hλ9229, Hλ3771/Hλ9229, Hλ3835/Hλ9229, Hλ4102/Hλ9229, Hλ4340/Hλ9229, Hλ4861/Hλ9229, and Hλ6563/Hλ9229), to exclude ratios affected by flux calibration issues. Finally, each measured emission line flux is corrected for extinction using Eq. (1), where the correction term is acquired with PYNEB's *getCorr* function (Luridiana et al. 2015). The E_{B-V} as shown in Fig. 3 is related to c(Hβ) as

$$(1 - f(\lambda))\ \mathrm{c}(\mathrm{H}\beta) = 0.4\ E_{B-V}\ X(\lambda), \qquad (2)$$

where $X(\lambda) = A(\lambda) / E_{B-V} = R_V A(\lambda) / A_V$. The mean E_{B-V} for the resolved view is 0.34 ± 0.01. A map of the reddening corrected Hα flux together with its radial profile can be seen in Fig. 4.

3.2. Calculation of physical properties

3.2.1. Electron densities

The calculation of electron density, temperature, and ionic abundances was also done with the PYNEB package. To measure the resolved electron density, we used the common ratios of the two CEL line doublets: [S II]λ6717/λ6731 and [O II]λ3727/λ3729, together with the PYNEB *getTemDen* function. An initial guess of 10 4000 K for the electron temperature was used in this step. To get a stable measurement for the densities and associated uncertainties of our measurement, we executed 1000 Monte Carlo (MC) realizations of these calculations, adding random noise to the initial flux values in each realization. This random noise ranges between zero and the uncertainty of the initial flux measurements. The final density values were taken as the median of the 1000 MC results, whereas the uncertainties result from the MC standard deviation. Because this process would result in a huge amount of computing time when done for each spaxel, the machine learning tool AI4NEB[2] was used to accelerate the computations. In this approach, a neural network is first trained on examples of line ratios together with their corresponding T_e and n_e values and is then applied to predict the physical parameters directly from the observations.

3.2.2. Electron temperatures

For the measurement of the resolved electron temperatures, we used the common ratios of temperature-sensitive lines: [N II]λ6584/λ5755, [O II]$\lambda\lambda$(3727+3729)/λ7320[3], [S II]$\lambda\lambda$(6717+6731)/λ4069, and [S III]λ9531/λ6312. In this step, we used PYNEB's *getTemDen* function with a density value taken to be the mean of our two density measurements, n_e([O II]) and n_e([S II]). We note that using either n_e([O II]), n_e([S II]), or the mean value does not significantly affect the resulting electron temperatures and abundances. Similar to the density calculations, 1000 MC realizations were executed using AI4NEB and the final temperature measurements were calculated as the median of those realizations.

The measurement of T_e([S II]) needs to be handled with caution as there might be inaccurate or excessive sky subtraction in the [S II]λ4069 line, potentially leading to an overestimation of the temperatures. For this reason, we did not use this diagnostic in further calculations of the abundances. We also attempted to calculate the electron temperatures using the [Ar III]λ7135/λ5192 and [O III]λ5007/λ4363 ratios. However, the fainter emission lines that are required for these diagnostics (e.g., [Ar III]λ5192, [O III]λ4363) were not measured with S/N > 3 in a sufficient number of fibers.

3.2.3. Abundances

To measure the resolved ionic abundances of oxygen, we used PYNEB's *getIonAbundance* function together with the mean electron density value. For the calculation of the O^+ abundance, we used the [O II]$\lambda\lambda$3727+3729 lines together with the mean temperature of the low-ionization states T_e([N II]) and T_e([O II]). We excluded the T_e([S II]) measurement from this calculation, as its values might be overestimated (see Sect. 4.2). For the calculation of the O^{2+} abundance, we used the [O III]λ5007 line together with the electron temperature for high-ionization states, T_e([S III]). We could not use the temperature of [O III] as the λ4363 line is not detected. As before, the use of different density or temperature diagnostics for the abundance determination does not significantly affect the final abundance values. A similar MC run as above was carried out for these measurements, with a lower number of 100 realizations, as the abundance calculations take a much longer time compared to the calculations of densities and temperatures.

3.3. Integrated measurements

In order to quantify the differences between spatially resolved and unresolved measurements of electron density, temperature, and oxygen abundance, and constrain the impact of inhomogeneities, we construct an integrated spectrum by co-adding all fiber spectra from the full LVM pointing into a single spectrum on which the emission line analysis is performed. Although

[2] https://github.com/Morisset/AI4neb

[3] We did not include λ7330, as it blends with an OH airglow sky line producing emission around λ7330 evident from the double peak and broader shape compared to λ7320 in Fig. 2.

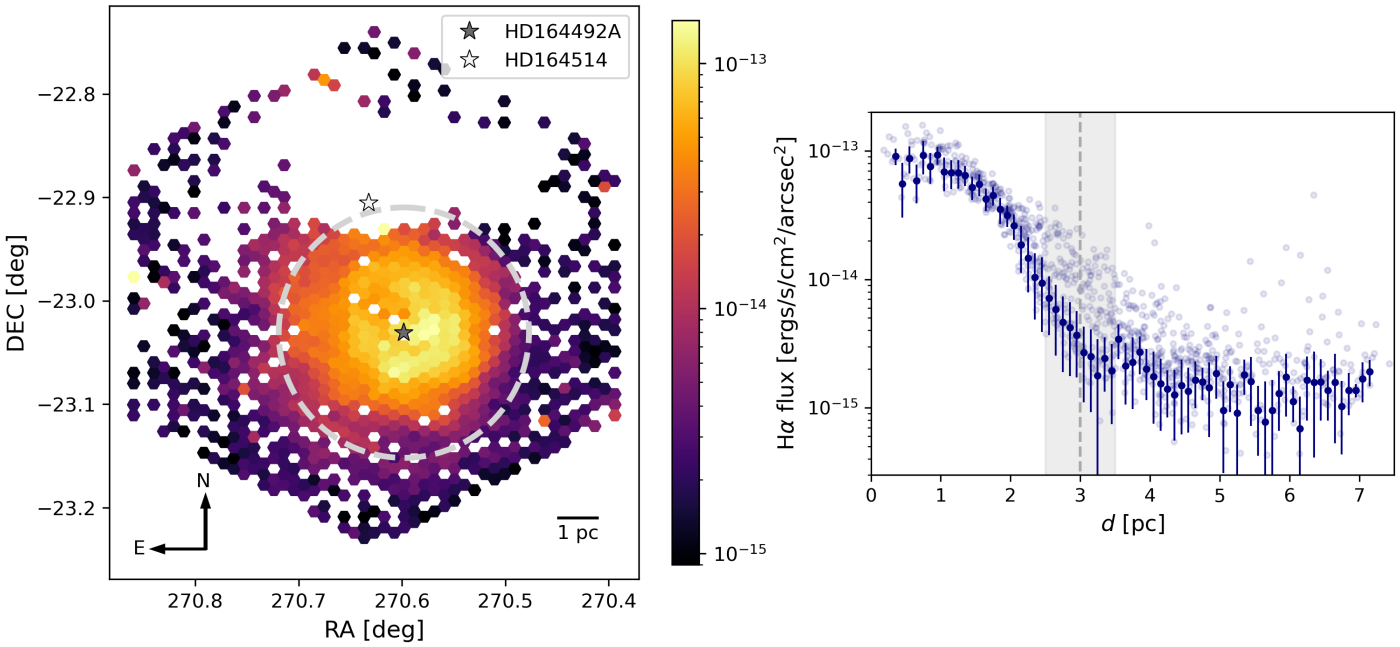

Fig. 4. *Left*: map of the reddening corrected Hα line flux as described in Sect. 3.1. The position of HD 164492A is marked with a grey star, while the position of HD 164514 is marked with a white star. The extent of the measured Strömgren sphere (Sect. 3.4) is shown by a grey dashed circle. *Right*: radial variation of the reddening corrected Hα line flux as a function of the distance to the ionizing star HD 164492A. Faint points represent individual spaxels, while opaque points show the uncertainty-weighted average of all spaxels within 0.1 pc wide distance bins. Standard deviations are shown as error bars. The extent of the measured Strömgren sphere (Sect. 3.4) is shown by a grey dashed line together with the error as a grey shaded region.

we could restrict the integration to the fibers located within a sphere around HD 164492A, we adopt the full tile integration to better mimic extragalactic observations, where individual H II regions cannot typically be resolved and the integrated spectrum naturally includes surrounding diffuse emission and unrelated structures. We also verified that restricting the integration to a sphere with 2.43 pc radius (the theoretical Strömgren radius of an O 7.5 V star) does not significantly alter the derived physical parameters. A collection of strong and weak lines observed with the full integrated spectrum is shown in Fig. 2, and the measured line fluxes can be found in Appendix A.

The same analysis as described in Sects. 3.1 and 3.2 is then repeated on the integrated spectrum. Using the same hydrogen line ratios as for the resolved measurements, we get $E_{B-V} = 0.36 \pm 0.01$. The improved S/N of the integrated spectra also allows us to measure the electron temperature from the ratio of the He I λ7281/λ6678 recombination lines (Zhang et al. 2005; Méndez-Delgado et al. 2025). Because this is not a standard CEL-diagnostic in PYNEB, we define a function that takes the observed line ratio and returns the corresponding electron temperature. For this, we calculate the theoretical emissivity ratios for various possible temperatures in the range of 5000–20 000 K and use SCIPY's *interp1d* to construct an interpolation function that lets us constrain T_e(He I). As with previous measurements, we repeat the calculation of the helium electron temperature for 1000 MC realizations, take the mean value as our final result, and the standard deviation as an uncertainty estimate.

3.4. Estimating the stellar ionizing rate Q_0

Because the Trifid Nebula is only ionized by a single O-star HD 164492A, it shows a rather simple ionization structure in which we can probe spherical symmetries. The Hα flux as seen in Fig. 4 shows azimuthal variations smaller than 10%.

The ionization equilibrium implies that, for a filled sphere of gas, the rate of photoionizations is balanced by the rate of recombinations (Osterbrock 1974; Draine 2011), expressed as

$$Q_0[s^{-1}] = \frac{4}{3}\,\pi\,\mathrm{R}^3\,f_{\mathrm{fill}}\,\mathrm{n}_e^2\,\frac{\alpha_B}{f_{H^+}}, \tag{3}$$

where Q_0 is the number of ionizing photons emitted by the central source, R is the size of the considered sphere (it may be the Strömgren radius if the region is radiation-bounded), f_{fill} is the filling factor (or clumpiness factor), n_e is the electron density, α_B is the case B recombination coefficient, and f_{H^+} is the fraction of ionizing photons that actually ionize H (and not dust or other elements; the covering factor $\Omega/4\pi$ also enters in f_{H^+}, as well as the escaping fraction due to a matter-bounded nebula). The case B recombination coefficient can be expressed by:

$$\alpha_B[\mathrm{cm}^3\ \mathrm{s}^{-1}] = 2.59 \times 10^{-13}\ \mathrm{T}_4^{-0.833-0.034\ \ln(\mathrm{T}_4)}, \tag{4}$$

following Table 14.1 from Draine (2011), where $\mathrm{T}_4 = \mathrm{T}_e/10^4\mathrm{K}$.

The value of Q_0 can then be estimated from the observations presented in this work. From the resolved Hα flux in Fig. 4 (right), we can see that the flux is high in the central region and decreases heavily until a distance of around 3.0 pc. This sets our observed radius to $\mathrm{R}_{\mathrm{obs}} = 3.0 \pm 0.5$ pc. The main difficulties are to determine the filling factor, f_{fill}, and the electron density, n_e. The latest derived from the [S II]λ6717/λ6731 line ratio seems to decrease with the distance to the center, as shown in Fig. 6 described below. This only gives insights into the low ionization region density; the inner, higher ionization part of the nebula may be at higher densities. A way to remove these difficulties is to consider the integrated flux Hα, which can be expressed as,

$$L\,(\mathrm{H}\alpha)\ [\mathrm{erg\ s}^{-1}] = \frac{4}{3}\,\pi\,\mathrm{R}^3\,f_{\mathrm{fill}}\,\mathrm{n}_e^2\,\epsilon_\alpha, \tag{5}$$

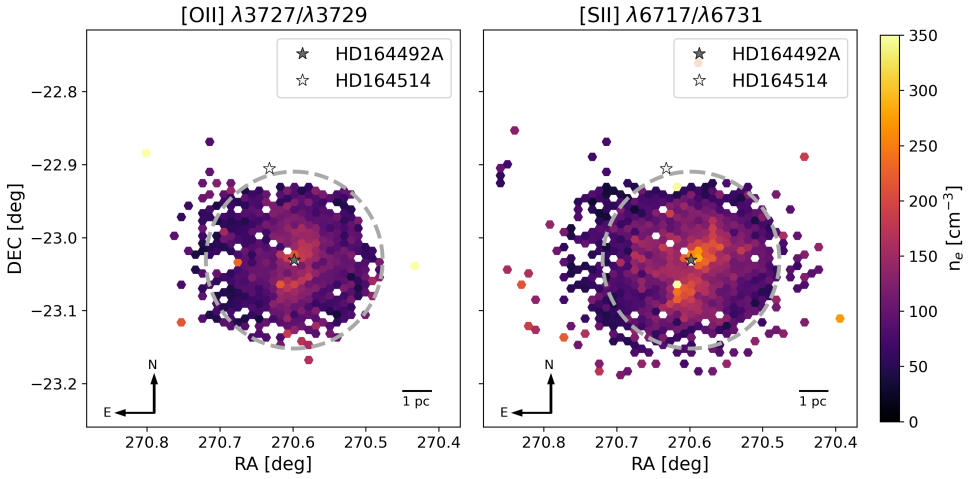

Fig. 5. Maps of the electron densities. In all maps, the position of HD 164492A is marked with a grey star, while the position of HD 164514 is marked with a white star. The extent of the measured Strömgren sphere (Sect. 3.4) is shown by a grey dashed circle. Uncertainty maps corresponding to each density tracer are shown in Fig. D.2.

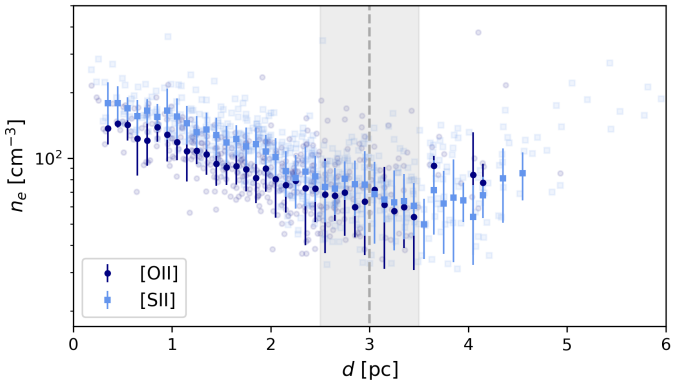

Fig. 6. Radial variation of the electron densities (n_e([O II]) in dark blue circles and n_e([S II]) in light blue squares) as a function of the distance to the ionizing star HD 164492A. Faint points represent individual spaxels, while opaque points show the uncertainty-weighted average of all spaxels within 0.1 pc wide distance bins. Standard deviations are shown as error bars. The extent of the measured Strömgren sphere (Sect. 3.4) is shown by a grey dashed line together with the error as a grey shaded region.

where ϵ_α, the emissivity of Hα, is taken from Eq. (14.8) of Draine (2011), expressed as

$$\epsilon_\alpha \text{ [erg s}^{-1}\text{ cm}^3\text{]} = h\,\nu_\alpha\,\alpha_{\text{eff, H}\alpha} = 3.55\times10^{-25}\,T_4^{-0.942-0.031\,\ln(T_4)}. \quad (6)$$

Together with Eqs. (3) and (5), this leads to the following relation:

$$Q_0\text{ [s}^{-1}\text{]} = L(\text{H}\alpha)\,\frac{\alpha_B(T_e)}{\epsilon_\alpha(T_e)\,f_{H^+}} = 7.32\times10^{11}\text{[erg}^{-1}\text{]}\,L(\text{H}\alpha)\text{ [erg s}^{-1}\text{]}\,\frac{T_4^{0.1}}{f_{H^+}}, \quad (7)$$

where for T_e = 10 000 K, the exponent of T_4 simplifies to 0.1. The only parameter to be determined remains f_{H^+}.

The integrated spectrum over all LVM spaxels allowed us to define L(Hα). We used the distance to the Trifid Nebula of d =1.42 $^{+0.09}_{-0.08}$ kpc (see Sect. 1) to calculate the Hα luminosity, L(Hα), on the basis of the observed integrated and reddening corrected Hα flux, F (Hα), using

$$L(\text{H}\alpha)\text{ [erg s}^{-1}\text{]} = 4\pi\,(d\text{ [cm]})^2\;F(\text{H}\alpha)\text{ [erg s}^{-1}\text{ cm}^{-2}\text{]} \times\frac{1}{f_{\text{LVM}}}, \quad (8)$$

where f_{LVM} is the fill factor of the LVM fibers of 0.83 as mentioned in Sect. 2. The value we obtained is L(Hα) = (8.66 ± 0.5) × 10^{36} erg/s.

Using Eq. (7) in the case of a pure hydrogen nebula of constant n_e = 95 cm^{-3} with f_{H^+} = 1 and at T_e = 8600K, we obtained Q_0 = (6.25 ± 0.36) × 10^{48} s^{-1}; then, with Eq. (3) and f_{fill} = 1, we obtained a radius of R = 2.7 ± 0.3 pc. A filling factor of f_{fill} = 0.7 is needed to recover a Strömgren radius of 3.0 pc.

To determine a value of f_{H^+} more tailored to the Trifid conditions, we ran a photoionization toy model using the CLOUDY code (v25.00, see Gunasekera et al. 2025), applying a more realistic ionizing flux distribution, a decreasing electron density law, dust mixed with the ionized gas, and a filling factor, f_{fill} = 0.73 (computational details can be found in Appendix B). The resulting value for f_{H^+} is 0.35, leading to Q_0 = 2.09 × 10^{12} L(Hα) = (1.8 ± 0.1) × 10^{49} s^{-1}. This must be considered as a lower value, as the model describes a radiation-bounded nebula, with a complete covering factor.

4. Results

4.1. Spatially resolved electron densities

The electron density maps in Fig. 5 show a similar overall structure for both measured line ratios, with higher densities around 150 cm^{-3} for n_e([O II]) to 200 cm^{-3} for n_e([S II]) in the central region near the ionizing source. Both maps indicate a decrease in density with increasing distances from the central ionizing star HD 164492A to a minimum of around 30 cm^{-3} for n_e([O II]) and 40 cm^{-3} for n_e([S II]). This negative radial gradient in density is also clearly visible in Fig. 6, showing the radial density distribution, where the density minimum is reached at a distance of approximately 3–4 pc from the center. It can also be seen that the electron density measured with the [O II] doublet is systematically lower by approximately 10–50 cm^{-3} than the n_e([S II]) measurement, which can be explained by the fact that the two diagnostics have different critical densities, leading to small systematic offsets.

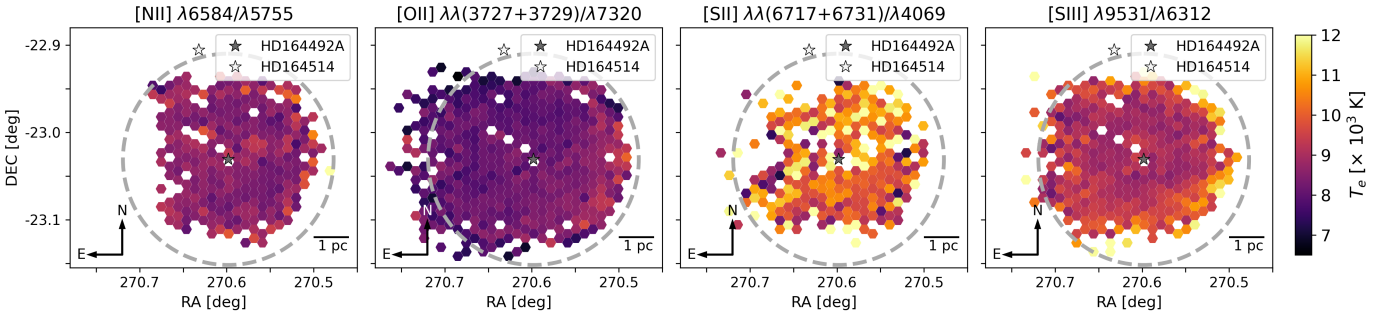

Fig. 7. Maps of electron temperatures from different diagnostics. In all maps, the position of HD 164492A is marked with a grey star, while the position of HD 164514 is marked with a white star. The extent of the measured Strömgren sphere (Sect. 3.4) is shown by a grey dashed circle. Uncertainty maps corresponding to each temperature tracer are shown in Fig. D.3.

Table 1. Results of the integrated measurements together with the mean values of the resolved calculations.

Property	Spectrum	Value	Unit
n_e([O II])	Integrated	95 ± 16	cm^{-3}
	Resolved	85 ± 30	
n_e([S II])	Integrated	103 ± 7	cm^{-3}
	Resolved	97 ± 37	
T_e([N II])	Integrated	8805 ± 909	K
	Resolved	8541 ± 382	
T_e([O II])	Integrated	7677 ± 311	K
	Resolved	8180 ± 324	
T_e([S II])	Integrated	11207 ± 1420	K
	Resolved	10024 ± 905	
T_e([S III])	Integrated	9357 ± 544	K
	Resolved	9035 ± 374	
T_e(He I)	Integrated	11417 ± 3292	K
12+log(O/H)	Integrated	8.49 ± 0.14	
	Resolved	8.47 ± 0.09	
12+log(O^+/H)	Integrated	8.46 ± 0.15	
	Resolved	8.46 ± 0.12	
12+log(O^{2+}/H)	Integrated	7.31 ± 0.10	
	Resolved	7.38 ± 0.27	
Q_0	Integrated	1.8 ± 0.1	× 10^{49} s^{-1}

At larger distances, the overall [S II] density seems to increase again towards the outer edges of the LVM pointing, but these values also have uncertainties larger than 100 cm^{-3} (see Fig. D.2). Because of a lower S/N in the [O II] lines, we do not cover much of these fainter outer regions with the [O II] density measurement. Thus, the apparent increase in density might be an artifact of large uncertainties in the outer regions, although we cannot exclude a contribution from the reflection nebula, which could affect the observed line ratios and mimic a density enhancement.

The radial density variation in Fig. 6 shows a small increase in densities around 1 pc away from the central star, for both diagnostics. This increase is associated with a higher density concentration (at RA ≈ 270.61° and Dec ≈ −23.07°) that is visible to the south-east of HD 164492A in Fig. 5. Another region of enhanced electron density (at RA ≈ 270.58° and Dec ≈ −23.02°) can be seen north-west and very close to the ionizing star in Fig. 5, causing the highest density values of the most central part in Fig. 6.

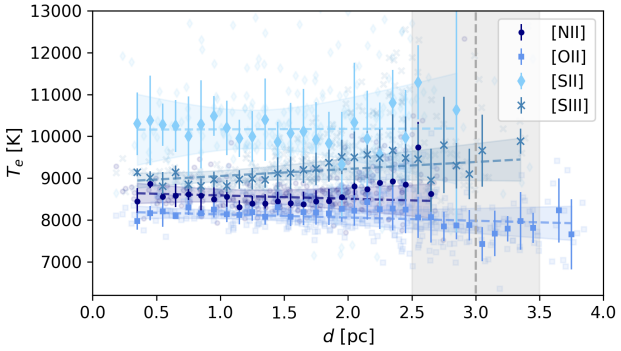

Fig. 8. Radial variation of the electron temperatures (T_e([N II]) in dark blue circles, T_e([O II]) in blue squares, T_e([S II]) in light blue diamonds, and T_e([S III]) in blue crosses) as a function of the distance to the ionizing star HD 164492A. Faint points represent individual spaxels, while opaque points show the uncertainty-weighted average of all spaxels within 0.1 pc wide distance bins. Standard deviations are shown as error bars. The extent of the measured Strömgren sphere (Sect. 3.4) is shown by a grey dashed line together with the error as a grey shaded region. The linear fits (slopes can be seen in Eq. (C.4)) to the single temperatures are displayed as dashed lines together with the 3σ uncertainties as shaded regions in the corresponding colors.

4.2. Spatially resolved electron temperatures

Spatially resolved maps of the electron temperatures measured through different diagnostic line ratios can be seen in Fig. 7, while uncertainties of these maps can be seen in Fig. D.3. In most maps, no clear structures or radial gradients can be found; only T_e([S III]) might give rise to a positive radial temperature gradient, but the scatter and uncertainties across these outer edges are also large (>1000 K, see Fig. D.3). On average, the measured T_e([N II]) and T_e([O II]) are lowest with mean values of 8541 ± 382 K and 8180 ± 324 K, respectively, while the T_e([S II]) values are highest with a mean of 10024 ± 905 K. The measured T_e([S III]) shows values in between the other diagnostics with a mean electron temperature of 9035 ± 374 K. All the mean values referenced here are reported in Table 1. Missing spaxels in the maps, especially in the T_e([S II]) distribution, result from low S/N in the [S II]λ4069 line, which leads to poor Gaussian fits that were subsequently discarded (see Sect. 2). This effect occurs in all temperature maps but is most pronounced for [S II] due to the weakness of the auroral line.

Looking at the radial electron temperature trends in Fig. 8, the different temperature regimes of the diagnostics become even clearer, with T_e([O II]) < T_e([N II]) < T_e([S III]) < T_e([S II]). To test their homogeneity, we also fitted linear functions to all

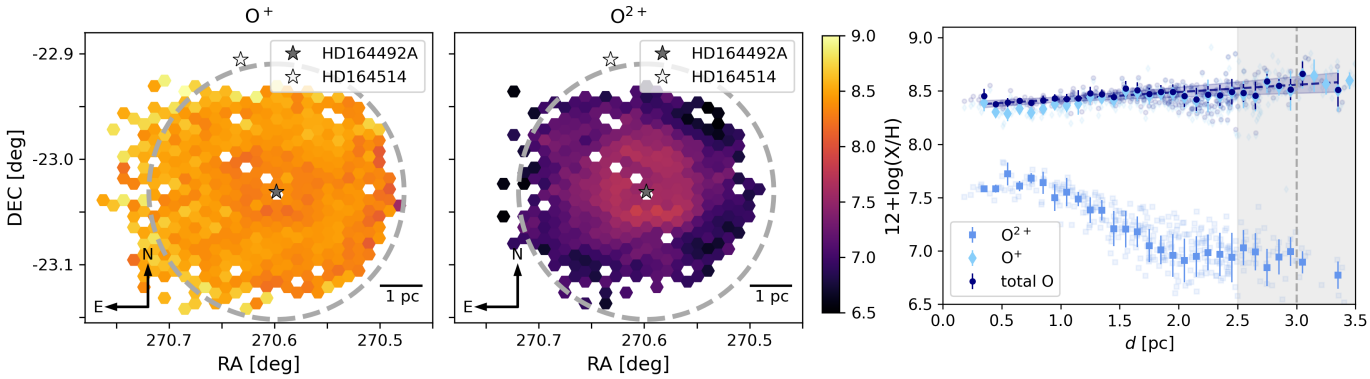

Fig. 9. *Left*: maps of the O^+ (left) and O^{2+} (right) abundances. In both maps, the position of HD 164492A is marked with a grey star, while the position of HD 164514 is marked with a white star. The extent of the measured Strömgren sphere (Sect. 3.4) is shown by a grey dashed circle. Uncertainty maps can be seen in Fig. D.4. *Right*: radial variation of the oxygen abundances (O^+ in light blue diamonds, O^{2+} in blue squares and the total O abundance in dark blue dots) as a function of the distance to the ionizing star HD 164492A. Faint points represent individual spaxels, while opaque points show the uncertainty-weighted average of all spaxels within 0.1 pc wide distance bins. Standard deviations are shown as error bars. The extent of the measured Strömgren sphere (Sect. 3.4) is shown by a grey dashed line together with the error as a grey shaded region. The linear fit (slope can be seen in Eq. (C.5)) to the total oxygen abundance is displayed as a dashed line together with the 3σ uncertainty as a shaded region.

temperatures with a least-squares algorithm (resulting gradients can be found in Appendix C). However, considering the uncertainties per spaxel and the 3σ confidence band from the fits (shaded regions in Fig. 8) into account, which can be of the order of 1000 K, especially at the outer edges, there is consistency with a flat temperature distribution. Also, azimuthal variations in electron temperatures are at maximum about the size of the measurement uncertainties. Given that T_e([S II]) is systematically higher than the other diagnostics, we interpret it as an upper limit on the true electron temperature. The reason for this systematic overestimation could be an inaccurate sky subtraction in the [S II]λ4069 line or an unresolved blending with the near [O II]λ4069.89 line.

Furthermore, we can directly estimate the amount of temperature variations across the plane of the sky by using Eq. (12) from Peimbert (1967), originally for a 3D nebula but here for the 2D projection of the sky plane,

$$t^2_{\rm ps} = \frac{\langle (T_e\,[\rm K] - T_0\,[\rm K])^2 \rangle}{T_0\,[\rm K]^2}, \tag{9}$$

where $t^2_{\rm ps}$ is a parameter for temperature fluctuations across the plane of the sky, T_0 is the mean electron temperature, and T_e is the local electron temperature. Applying this to the electron temperature gradients given above, we calculate: $t^2_{\rm ps}$([N II]) = (8.5 ± 1.2) × 10^{-5}, $t^2_{\rm ps}$([O II]) = (8.6 ± 1.0) × 10^{-5}, $t^2_{\rm ps}$([S II]) = (4.3 ± 0.6) × 10^{-4}, and $t^2_{\rm ps}$([S III]) = (2.0 ± 0.2) × 10^{-4}. These values indicate that the temperature fluctuations are very small, close to zero, consistent with what is seen directly in the temperature maps (see Fig. 7).

4.3. Spatially resolved oxygen abundance

Maps of the oxygen abundances and radial oxygen abundance trends are presented in Fig. 9. It can be seen that the overall abundance of O^+ is much higher than that of O^{2+}, indicating a low level of ionization in the nebula. Moreover, the abundance of O^{2+} shows a pronounced negative radial gradient with a higher abundance of ∼7.5 in the central regions, where we expect the high ionization zone, and lower values ∼7.0 in the outer regions. The abundance of O^+ exhibits the opposite trend, with values around 8.4 in the central region to abundances around 8.6 in the outer region, where we expect the low-ionization zone. This behavior of the O^{2+} and O^+ abundances neatly delineates the two ionization zones of the Trifid Nebula: the high-ionization zone up to a distance of around 1.8 pc from the central ionizing source and the low-ionization zone at distances larger than 1.8 pc (see also Fig. 9).

Analogous to the electron temperatures discussed in Sect. 4.2, the total oxygen abundance was fitted with a linear function (resulting gradient can be found in Appendix C). When considering both the 3σ fit uncertainty and the typical uncertainties of individual spaxels (approximately 0.1 dex, see Fig. D.4), any positive radial gradient cannot be robustly established. Azimuthal variations are also smaller than the measurement uncertainties, further supporting a largely homogeneous abundance distribution. The slight apparent trend may reflect variations in the electron temperature used to determine the O^+ abundance. While the electron temperature gradients were found to be relatively flat within the uncertainties, here they could contribute to the inferred metallicities ranging from 8.4 in the inner regions to 8.6 in the outskirts. Such a difference cannot be explained by dust depletion alone, which at solar metallicity accounts for only ∼0.1 dex (Mesa-Delgado et al. 2009). Overall, the total oxygen abundance appears approximately flat and homogeneous across the nebula, and any apparent gradient should be interpreted with caution, particularly given the uncertainties in T_e([N II]) and T_e([O II]).

4.4. Integrated physical properties

Table 1 presents the results for the physical properties of the integrated spectrum (see Sect. 3.3), alongside the mean values from the resolved measurements. Both sets are compared directly below.

Looking at the different measurements of the electron density, we can see that both views are consistent, given their uncertainties. The electron temperatures from resolved and integrated data match within 1σ for all diagnostics. Using the integrated spectrum, we were also able to calculate the helium temperature T_e(He I) = 11417 ± 3292 K. While the nominal value of this recombination line measurement is somewhat higher than the integrated temperatures of T_e([N II]), T_e([O II]), and

T_e([S III]), it is still consistent with those temperatures, given the uncertainties. The Heλ7281 line is well fitted, and no clear blend is visible, although a minor contribution from a residual sky line cannot be entirely ruled out, which could slightly increase the measured flux and thus the derived temperature. Moreover, the He I emission lines may be affected in cases where the assumption of pure Case B recombination does not hold, as discussed in Méndez-Delgado et al. (2025). Deviations from Case B conditions can arise due to the absorption of He I photons by neutral hydrogen, or as a result of general leakage of ionizing photons from the nebular region. The integrated and mean value of the resolved oxygen abundance are nearly identical with 8.49 ± 0.14 and 8.47 ± 0.09, respectively.

5. Discussion

Our IFU mapping reveals the full two-dimensional structure of the nebula. Below, we discuss the fully recovered density, temperature, abundance, and ionizing structures.

5.1. Density structure

Our spatially resolved electron density maps of the Trifid Nebula provide one of the most detailed views to date of its internal density structure, revealing both the expected radial gradient and discrete, compact density enhancements, and, for the first time, allowing a direct comparison between resolved and integrated densities in this region.

The measurements of the electron densities, reflecting a line-of-sight average of the single-ionized zone, show a negative radial gradient as well as some discrete regions of enhanced density (see Sect. 4.1). The inner double-ionized region remains unprobed as it lacks a direct diagnostic. A negative radial density gradient was expected and also previously observed for other compact H II regions (e.g., Binette et al. 2002; Osterbrock & Ferland 2006; McLeod et al. 2016; Jin et al. 2023). There, clear negative slopes between −45 and −850 cm^{-3}/pc were measured in Jin et al. (2023), while McLeod et al. (2016) reported slopes of −2000 to −100 cm^{-3}/pc and slopes in Binette et al. (2002) can be as extreme as −2000 cm^{-3} per 0.1 pc. Electron density slopes in our measurements range between −50 and −20 cm^{-3}/pc. Such declining density profiles are consistent with expanding H II regions, where the ionized gas disperses the remnant molecular material (Geen et al. 2015).

We identify two unresolved clumps of enhanced density. The higher-density region south-east of HD 164492A (RA ≈ 270.61°, Dec ≈ −23.07°, Fig. 5) is also seen in maps from Kuhn et al. (2022), where a notably higher dust column density was measured compared to other regions in the nebula. This enhancement spatially corresponds to the TC 2 molecular column (Hester et al. 2004; Rho et al. 2008), a large collection of molecular gas exposed to ionizing photons. The resulting ionization produces free electrons, which we detect as higher electron densities. A similar mechanism could explain the high electron density north-west of the ionizing star (RA ≈ 270.58°, Dec ≈ −23.02°, Fig. 5), also reported as an obscured high-density region by Copetti et al. (2000) and spatially associated with a dense dust concentration (see Fig. 1). These compact, high-density structures probably represent remnants of the original molecular cloud being eroded by the advancing ionization front.

Overall, our measurements agree well with the literature's long-slit measurements, but provide a more complete and comprehensive view of the nebula. Comparing the absolute values of electron density, García-Rojas et al. (2006) measured n_e([O II]) = 240 ± 70 cm^{-3} and n_e([S II]) = 320 ± 130 cm^{-3} close to the ionizing star. Moreover, Copetti et al. (2000) measured a median n_e([S II]) of 161 cm^{-3} and a maximum of around 330 cm^{-3} using multiple long-slit positions also close to the center of M 20. As both studies used long-slit observations very close to the central ionizing star (less than 0.14 pc in distance, which is 0.10 pc lower than our spatial resolution), their results probe conditions in the immediate stellar environment, whereas our integrated and mean resolved values characterize a much more extended part of the nebula. The two approaches, therefore, trace different spatial scales and are not directly comparable. Instead, we will compare to the electron densities we see closest to the long-slit position, with values of: n_e([O II]) = 216 ± 33 cm^{-3} and n_e([S II]) = 257 ± 25 cm^{-3}, which are in the 1σ range. A study by Rodríguez (1999) measured the [S II] electron density with three long-slit positions in the south-east direction, farther away from the center. Their first slit position is very close to the TC 2 molecular cloud and shows an electron density of 360 cm^{-3}, where we reach in the corresponding spaxel a similar value of n_e([S II]) = 359 ± 37 cm^{-3}. The second long-slit was placed north-east of TC 2, measuring 120 cm^{-3}. There we measure a density of n_e([S II]) = 157 ± 19 cm^{-3}, being in the 2σ range. A third slit measured an electron density of 340 cm^{-3} south of the ionizing star and south-west of TC 2 inside a dusty filament, where we reach a much lower value of n_e([S II]) = 217 ± 22 cm^{-3} outside the 3σ range. However, Rodríguez (1999) did not provide uncertainties to their measured values, limiting the comparison.

Assessing the impact of inhomogeneities on the integrated measurement, we find no significant discrepancy between our resolved and integrated density measurements in the Trifid Nebula. Such a direct comparison is rare and provides a valuable perspective on how local structures influence global nebular diagnostics. The observed density distribution of M 20 is consistent with evolving H II regions in a dense, clumpy molecular environment. The combination of smooth radial gradients and compact density peaks likely reflects ongoing photo-evaporation and the gradual dissolution of the original molecular and dusty structures.

5.2. Temperature structure

Our spatially resolved electron temperature measurements of M 20 provide the first detailed two-dimensional view of thermal conditions across the nebula, enabling a direct assessment of temperature homogeneity, a resolved comparison with integrated values, and a new spatial approach to estimating temperature inhomogeneities using t^2_{ps}.

Despite targeting potential temperature inhomogeneities, our measurements of the electron temperature (see Sect. 4.2) reveal remarkably homogeneous conditions without any significant radial gradients. Compared to the more extended H II regions typically targeted in extragalactic studies, a compact region such as M 20 would be unresolved and easily blended with diffuse ionized gas in the integrated spectra of external galaxies. This also suggests that temperature inhomogeneities may not be present, or at least not significant, in all types of H II regions.

Although outwardly increasing temperatures might be expected due to the penetration of high-energy ionizing photons into the outer regions of the nebula (Osterbrock & Ferland 2006), the thermal balance is governed not only by heating but also by spatially varying cooling processes. In particular, changes in the ionization structure can substantially affect the local cooling

rates. As a result, only detailed photoionization models can determine whether the electron temperature increases or decreases with radius. In the case of a model as described in Appendix B, a slight outward increase in electron temperature is predicted. The lack of a temperature rise at larger distances from the central ionizing star may result from higher uncertainties (>1000 K, see Fig. D.3) in the outermost spaxels. But, as mentioned above, positive gradients in electron temperature are not crucial for H II regions and homogeneous temperatures are also measured e.g., four H II regions in the Large and Small Magellanic Clouds (Jin et al. 2023).

Now we compare our individual electron temperature measurements to those reported in the literature, particularly focusing on the work of García-Rojas et al. (2006) and Rodríguez & Rubin (2005). For the [N II] temperature, García-Rojas et al. (2006) reported T_e([N II]) = 8375 ± 400 K close to the nebular center. Our measured value of T_e([N II]) = 9351 ± 597 K is consistent within 2σ. Similarly, for [O II], García-Rojas et al. (2006) found T_e([O II]) = 8275 ± 350 K, while we measure T_e([O II]) = 8144 ± 191 K, which is in agreement within 1σ. For [S II], García-Rojas et al. (2006) reported T_e([S II]) = 6950 ± 350 K, while we measure T_e([S II]) = 8598 ± 1435 K, which is in agreement within 2σ. In the case of [S III], our measurement of T_e([S III]) = 9190 ± 423 K lies in the 2σ range with the value of 8300 ± 400 K reported by García-Rojas et al. (2006).

These discrepancies may arise from differences in observational data quality or analytical methodology. While LVM spectra have a resolution of R ∼ 4000, the long-slit spectra of UVES, used in García-Rojas et al. (2006), have R ∼ 8800. Also in their work, García-Rojas et al. (2006) used an R_V = 3.1 and a Seaton reddening law (Seaton 1979) while we use R_V = 5.5 and the modified Cardelli law (Cardelli et al. 1989; Blagrave et al. 2007) as pointed out in Sect. 3.1. However, testing their reddening setup on our LVM data does not cause a significant change in the measured electron temperatures. Moreover, an updated set of atomic data was used in our calculations. The sum of these differences in the analysis could be responsible for major differences between these studies. We also compare our [N II] temperature measurements to those reported by Rodríguez (1999) at three different positions across the nebula. They report T_e([N II]) = 8500, 8300, and 8600 K, while our corresponding values are 8530 ± 401 K, 8773 ± 659 K, and 8646 ± 404 K, respectively. All of our measurements lie within the 1σ range of the values by Rodríguez (1999). However, Rodríguez (1999) did not quote uncertainties, limiting a stricter comparison.

Using radio recombination lines, Khan et al. (2024) measured electron temperatures as a function of the galactocentric radius and calculated a relation. Applying the galactocentric distance for M 20 of 6.79 kpc (Méndez-Delgado et al. 2022a), the expected electron temperature would be 7269 ± 1700 K. This value is in 1σ range with our resolved and integrated measurements of T_e([N II]) and T_e([O II]), and still in 2σ range of our measurements of T_e([S II]), T_e([S III]) and T_e(He I) (see Sect. 4.2 and Table 1). For all electron temperature measurements, the values of integrated and resolved views are all close and within the 1σ range.

Lastly, García-Rojas et al. (2006) calculated, using different methods, a t^2 value between 0.017 ± 0.010 and 0.049 ± 0.019, while most of our t^2_{ps} measurements are much smaller, and an order of 10^{-4}–10^{-5}. While García-Rojas et al. (2006) measured the inhomogeneity t^2 with different calculations of the electron temperature from long-slit observations (as these temperatures trace different physical zones within the nebula; see Sect. 1), we can infer it more reliably by directly using measured temperature gradients from spatially resolved LVM data across the plane of the sky.

5.3. The impact of inhomogeneities on the metallicity

Our spatially resolved abundance analysis enables, for the first time in M 20, a direct comparison between resolved and integrated metallicity measurements. This reveals how local inhomogeneities, or their absence, impact abundance determinations and provides new insight into the longstanding debate over gas versus stellar metallicities.

A main goal of this study was to understand the influence of density and temperature inhomogeneities on the measured metallicity in unresolved, integrated H II regions. Despite showing no relevant temperature inhomogeneities, our resolved measurements of the oxygen abundance seem to follow a slight positive radial gradient. But due to uncertainties, the radial gradient might be consistent with a flat profile. While our spatially resolved analysis shows that the density variation exceeds the temperature and abundance variations within M 20, the dominant source of inaccuracy for metallicity calibrations in unresolved extragalactic regions is likely the variation in ionization parameter and density structure (Kewley et al. 2019b; Méndez-Delgado et al. 2023a). The integrated spectra mix emission from high- and low-ionization zones as well as DIG, shifting strong-line ratios away from single-zone calibration relations. However, abundances measured with auroral line electron temperatures can also be affected by temperature inhomogeneities, but for typical extragalactic strong-line methods the ionization and density structure as well as DIG contamination drive the main systematic uncertainties.

Compared to other studies, our resolved and integrated measurements of the absolute oxygen abundance (8.47 ± 0.09 and 8.49 ± 0.14 respectively) are lower than the calculation of García-Rojas et al. (2006) which includes temperature inhomogeneities, resulting in a total oxygen abundance of 8.67 ± 0.03 (we only take into account the O^+ and O^{2+} abundance measurements to keep it most similar to our study). However, our measured abundances match well with the homogeneous approach by García-Rojas et al. (2006), resulting in a total oxygen abundance of 8.53 ± 0.03. When we compare the total oxygen abundance in the spaxel corresponding to the long-slit position of García-Rojas et al. (2006), our measurement is 8.39 ± 0.08. This value falls within the 2σ range of their result using the homogeneous approach, but lies outside the 3σ range when compared with their inhomogeneous assumption. We can also compare our results to the different long-slit positions of Rodríguez (1999). In the first slit position, the combined O^+ and O^{2+} abundance is 8.22, which is outside the 3σ range of our spaxel value of 8.44 ± 0.05. The third slit position shows a similar oxygen abundance of 8.20, while in the corresponding spaxel, we measure again 8.44 ± 0.05, which is also outside the 3σ range. Only in the second slit position with a value of 8.32, we are measuring 8.38 ± 0.08 and are within the 1σ range. However, similar to Sects. 4.1 and 4.2, Rodríguez (1999) did not give uncertainties for their measurements, which limits a qualitative comparison.

Comparing our measured mean resolved and integrated gaseous oxygen abundances to the stellar one of HD 164492A ($8.56\ ^{+0.3}_{-0.12}$, Martins et al. 2015), we find a good match between both abundance measurements. However, as the abundance measurement of O-stars is very difficult and leads to large

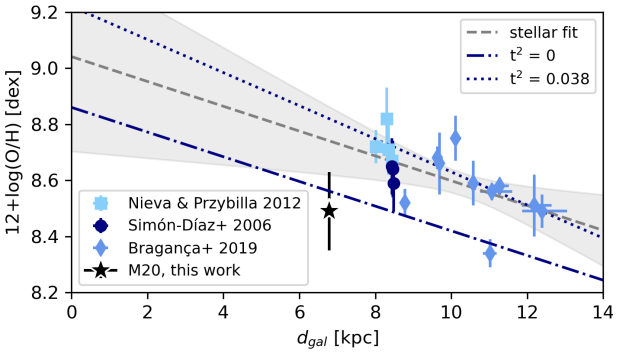

Fig. 10. Oxygen abundance trend calculated from B V-stellar measurements by Simón-Díaz et al. (2006); Nieva & Przybilla (2012); Bragança et al. (2019). The fit is illustrated by a grey dashed line, whereas the shaded region indicates the 3σ uncertainty of the fit. Fits from Méndez-Delgado et al. (2022a) for $t^2 = 0$ and $t^2 = 0.038$ are shown as dark blue dash-dotted and dotted lines, respectively. The position of the nebular oxygen abundance of M 20 calculated in this work (8.49 ± 0.14, from the integrated view) is indicated by the black star.

uncertainties, we also present in Fig. 10 a relationship between B-dwarf stellar abundances and the galactocentric radii. We used this method as a second approach, besides the directly measured oxygen abundance of HD 16642A by Martins et al. (2015), to gain another estimate of the expected stellar oxygen abundance in the Trifid Nebula. Therefore, we used measured oxygen abundances of B V stars by Simón-Díaz et al. (2006); Nieva & Przybilla (2012); Bragança et al. (2019) and distances for these objects as measured by Bailer-Jones et al. (2021). We fitted a linear relation to the distribution in an abundance-distance plane and derived the following relationship,

$$12 + \log(\mathrm{O/H}) = (-0.04 \pm 0.01)\,[\mathrm{dex/pc}]\,(d_{\mathrm{gal}} \pm 1.46)\,[\mathrm{kpc}] + (9.04 \pm 0.11), \quad (10)$$

where d_{gal} is the galactocentric distance of the object. Using Eq. (10), we derived for M 20 at a galactocentric distance of $6.79\ ^{+0.09}_{-0.08}$ kpc (Méndez-Delgado et al. 2022a) an oxygen abundance of 8.74 ± 0.04. It can be seen that the estimated abundance from B-dwarfs is over 0.2 dex higher than the one measured for HD 164492A and M 20. In principle, the oxygen abundance in massive stars (O and early B types) could be lower due to CNO-equilibrium processing. Also, we lack abundance measurements of B V stars at distances below 7 kpc, making the prediction much harder. If the stellar oxygen abundance was indeed higher than the measured gas abundance, this might suggest oxygen depletion into dust, consistent with the prominent dust lanes observed across M 20 (e.g., Fig. 1). Nevertheless, a discrepancy of 0.2 dex exceeds the expected contribution from dust depletion, which is limited to around 0.1 dex (Mesa-Delgado et al. 2009; Simón-Díaz & Stasińska 2011). For reference, the solar oxygen abundance is 8.69 ± 0.04 (Asplund et al. 2021), and it would be reasonable to assume that M 20 appears slightly more metal-rich than the Sun, given its location closer to the Galactic center.

When comparing our results to the oxygen abundance gradients obtained through multiple Galactic H II regions reported by Méndez-Delgado et al. (2022a) (their Table 2 and Fig. 4), we find good agreement with the gradient obtained assuming $t^2 = 0$. Although our measurement of M 20's oxygen abundance lies outside the 1σ range of the fit assuming $t^2 = 0.038$, this latter fit shows better agreement with the gradient derived from stellar abundances.

Interestingly, both the gas-phase and O-star abundances in M 20 are relatively low compared with the Galactic gradient traced by B-dwarfs and multiple H II regions (e.g., Méndez-Delgado et al. 2022a), as illustrated in Fig. 10. This raises the questions of whether M 20 reflects a local region of lower metallicity, potentially requiring an influx of relatively pristine gas or retaining signatures of its initial, less enriched environment. And if in such compact, relatively quiescent H II regions, we should not expect significant temperature inhomogeneities, which would be consistent with the remarkably homogeneous electron temperature we measure across M 20.

5.4. Exploring the ionization structure of M 20

Different approaches to estimating the amount of ionizing photons emitted by the central stellar source (see Sect. 3.4) yield different values. The measured value (using the tailored model) of $Q_0 = (1.8 \pm 0.1) \times 10^{49}$ s^{-1} is considerably higher than $Q_0 = 4.07 \times 10^{48}$ s^{-1} and $Q_0 = 7.6 \times 10^{48}$ s^{-1}, the theoretical ionizing rates of an O 7.5 V and an O 6.5 V star, respectively (Martins et al. 2005). Obtaining a lower Q_0 would require physical conditions that are considered unlikely for this system. However, our measured value matches well with the ionizing photon rate previously reported by Binder & Povich (2018) of $Q_0 = (1.5 \pm 0.4) \times 10^{49}$ s^{-1}. These discrepancies from the theoretical ionizing rates may be attributed to several factors, as detailed below.

The most straightforward interpretation of this discrepancy is that the ionizing source, HD 164492A, is likely of an earlier spectral type than the recent O 7.5 V classification suggests. The measured effective temperature by Martins et al. (2015) of 38 000 K leads to the assumption of an O 6.5 V star, while from our measurements, the ionizing flux is consistent with an O 5 V star (Martins et al. 2005). HD 164492 is also a complex multiple system including O 7 V, B 6 V, A 2 Ia, and possibly a Be star (Rho et al. 2004, 2006; Binder & Povich 2018), but these additional stars contribute negligibly to the total ionizing flux, as the earliest spectral type dominates by orders of magnitude (e.g., Ramachandran et al. 2019). Previous suggestions of binarity for HD 164492A (Stickland & Lloyd 2001) could affect the inferred spectral type, but searches for a companion remain inconclusive.

Moreover, prominent dust lanes are observed across the Trifid Nebula (Fig. 1), so inferring Q_0 from Hα under the assumption of a dust-free nebula would underestimate the true ionizing photon output (see Appendix B). Our CLOUDY toy model suggests that the difference between the classical Strömgren radius and the observed nebular size can be explained by the combined effects of dust opacity and density inhomogeneities. When compared to Kennicutt (1998), the higher ratio of $Q_0/L(\mathrm{H}\alpha) = 2.1 \times 10^{12}$ erg^{-1} obtained by the model further highlights the influence of dust, while regions with lower gas coverage may allow some ionizing photons to escape, so the nebula may not be fully radiation-bounded in all directions.

6. Conclusions

The Trifid Nebula (M 20), a compact, nearly spherical H II region, offers an ideal laboratory to study the internal physical structure of a simple Strömgren sphere ionized by the mid-type O-dwarf HD 164492A. Its simplicity in terms of ionizing structure, along with the presence of current star formation, makes

M 20 a benchmark system for testing ionization and abundance diagnostics.

We observed M 20 using the LVM as part of SDSS-V (Perruchot et al. 2018; Kollmeier et al. 2019; Drory et al. 2024; Blanc et al. 2024; Herbst et al. 2024; Kollmeier et al. 2025), which provides wide-field integral field spectroscopy with a resolution of R ∼ 4000 across 3600–9800 Å. With a spatial resolution of 0.24 pc, we spatially resolved the ionized gas and measured physical properties across the nebula.

Our spatially resolved measurements of the electron density, temperature, and oxygen abundance reveal a detailed internal view of the nebula. We identified a clear negative radial electron density gradient and two distinct clumps of enhanced density, each spatially coincident with dusty or molecular features (see Sect. 4.1). These structures likely result from interactions between ionizing photons and dense gas, highlighting the interplay between local environmental conditions and nebular structure.

In contrast, electron temperatures seem remarkably uniform across the nebula (see Sect. 4.2). This absence of a clear positive temperature gradient, which is often (but not always) expected from ionization theory, could be attributed in part to uncertainties in the outermost regions. However, it also depends on factors such as metallicity and the shape of the ionizing spectral energy distribution. However, it is consistent with findings in other homogeneous H II regions (e.g., Jin et al. 2023). Our spatially resolved approach allows us to estimate temperature inhomogeneities using the t^2 formalism (Peimbert 1967) directly from the measured gradients, revealing significantly lower values than those reported in long-slit studies.

When examining oxygen abundances, we find that resolved and integrated measurements agree closely, with weak evidence of a positive radial metallicity gradient (see Sect. 4.3). Our measurements are consistent with other homogeneous analyses in the literature (García-Rojas et al. 2006; Méndez-Delgado et al. 2022a) and lower than inhomogeneity-corrected estimates. Furthermore, we compare our nebular abundance to the stellar oxygen abundance of HD 164492A, finding general agreement. However, when comparing to an extrapolated oxygen abundance trend based on B-dwarfs, our derived oxygen abundance is about 0.2 dex lower than expected for the galactocentric distance of M 20.

The ionization structure of M 20 appears to exhibit a higher ionizing photon rate than would be expected from a single O 7.5 V star. This discrepancy likely reflects a combination of factors, including a possible misclassification of the central source HD 164492A, which may be an earlier-type or binary system, or other modeling assumptions about the physical conditions within the nebula. Our CLOUDY toy model further suggests that dust opacity and density inhomogeneities play a significant role in shaping the observed nebular size and ionization balance, indicating that M 20 is not fully radiation-bounded in all directions.

Overall, this study demonstrates the power of spatially resolved spectroscopy in disentangling the physical and chemical structure of Galactic H II regions. Our results show that integrated measurements can reliably trace average nebular conditions. Yet, even in cases of simple geometry, resolved maps reveal complex small-scale features and offer more direct insights into the role of local inhomogeneities. With the capabilities of LVM, we establish a framework for interpreting unresolved spectra of distant galaxies and for refining abundance diagnostics through detailed benchmarking in nearby star-forming regions such as the Trifid Nebula.

Acknowledgements. The authors thank the anonymous referee for the quick and helpful review. K.K., J.E.M.D., E.E., and N.S. acknowledge funding from the Deutsche Forschungsgemeinschaft (DFG, German Research Foundation) in the form of an Emmy Noether Research Group (grant number KR4598/2-1, PI: Kreckel) and the European Research Council's starting grant ERC StG-101077573 ("ISM-METALS"). J.E.M.D., C.M. and C.R.Z. thank the support by SECIHTI CBF-2025-I-2048 project "Resolviendo la Física Interna de las Galaxias: De las Escalas Locales a la Estructura Global con el SDSS-V Local Volume Mapper". C.M. acknowledges the support of the grant UNAM/DGAPA/PAPIIT IG101223. C.R.-Z. acknowledges support from grant UNAM-DGAPA-PAPIIT IG101723. E.J. acknowledges support from the interdisciplinary project Millennium Nucleus for the Evolutionary Reconstruction of the InterStellar medium (ERIS NCN2021_017). O.E. acknowledges funding from the Deutsche Forschungsgemeinschaft (DFG, German Research Foundation) – project-ID 541068876. A.A.C.S. is supported by the Deutsche Forschungsgemeinschaft (DFG, German Research Foundation) in the form of an Emmy Noether Research Group – Project-ID 445674056 (SA4064/1-1, PI: Sander). AACS further acknowledges funding by the Federal Ministry for Economic Affairs and Climate Action (BMWK) via the German Aerospace Center (Deutsches Zentrum für Luft- und Raumfahrt, DLR) grant 50 OR 2503 (PI: Sander). S.F.S. thanks the support by UNAM PASPA – DGAPA and the SECIHTI CBF-2025-I-236 project. J.G.F-.T gratefully acknowledges the grants support provided by ANID Fondecyt Postdoc No. 3230001 (Sponsoring researcher), and from the Joint Committee ESO-Government of Chile under the agreement 2023 ORP 062/2023. G.A.B. acknowledges the support from the ANID Basal project FB210003. Funding for the Sloan Digital Sky Survey V has been provided by the Alfred P. Sloan Foundation, the Heising-Simons Foundation, the National Science Foundation, and the Participating Institutions. SDSS acknowledges support and resources from the Center for High-Performance Computing at the University of Utah. SDSS telescopes are located at Apache Point Observatory, funded by the Astrophysical Research Consortium and operated by New Mexico State University, and at Las Campanas Observatory, operated by the Carnegie Institution for Science. The SDSS website is www.sdss.org. SDSS is managed by the Astrophysical Research Consortium for the Participating Institutions of the SDSS Collaboration, including Caltech, The Carnegie Institution for Science, Chilean National Time Allocation Committee (CNTAC) ratified researchers, The Flatiron Institute, the Gotham Participation Group, Harvard University, Heidelberg University, The Johns Hopkins University, L'Ecole polytechnique fédérale de Lausanne (EPFL), Leibniz-Institut für Astrophysik Potsdam (AIP), Max-Planck-Institut für Astronomie (MPIA Heidelberg), Max-Planck-Institut für Extraterrestrische Physik (MPE), Nanjing University, National Astronomical Observatories of China (NAOC), New Mexico State University, The Ohio State University, Pennsylvania State University, Smithsonian Astrophysical Observatory, Space Telescope Science Institute (STScI), the Stellar Astrophysics Participation Group, Universidad Nacional Autónoma de México, University of Arizona, University of Colorado Boulder, University of Illinois at Urbana-Champaign, University of Toronto, University of Utah, University of Virginia, Yale University, and Yunnan University.

References

Arthur, S. J., & Hoare, M. G. 2006, ApJS, 165, 283
Arthur, S. J., Medina, S. N. X., & Henney, W. J. 2016, MNRAS, 463, 2864
Asplund, M., Amarsi, A. M., & Grevesse, N. 2021, A&A, 653, A141
Bailer-Jones, C. A. L., Rybizki, J., Fouesneau, M., Demleitner, M., & Andrae, R. 2021, AJ, 161, 147
Baker, J. G., Menzel, D. H., & Aller, L. H. 1938, ApJ, 88, 422
Binder, B. A., & Povich, M. S. 2018, ApJ, 864, 136
Binette, L., González-Gómez, D. I., & Mayya, Y. D. 2002, Rev. Mexicana Astron. Astrofis., 38, 279
Blagrave, K. P. M., Martin, P. G., Rubin, R. H., et al. 2007, ApJ, 655, 299
Blanc, G. A., Morales, F., Besser, F., et al. 2024, SPIE Conf. Ser., 13094, 1309403
Bragança, G. A., Daflon, S., Lanz, T., et al. 2019, A&A, 625, A120
Cambrésy, L., Rho, J., Marshall, D. J., & Reach, W. T. 2011, A&A, 527, A141
Cardelli, J. A., Clayton, G. C., & Mathis, J. S. 1989, ApJ, 345, 245
Conroy, C., Weinberg, D. H., Naidu, R. P., et al. 2022, arXiv e-prints [arXiv:2204.02989]
Copetti, M. V. F., Mallmann, J. A. H., Schmidt, A. A., & Castañeda, H. O. 2000, A&A, 357, 621
Dopita, M. A., Seitenzahl, I. R., Sutherland, R. S., et al. 2019, AJ, 157, 50
Draine, B. T. 2011, Physics of the Interstellar and Intergalactic Medium (Princeton: Princeton University Press)
Drory, N., Blanc, G. A., Kreckel, K., et al. 2024, AJ, 168, 198
Esteban, C., Fang, X., García-Rojas, J., & Toribio San Cipriano, L. 2017, MNRAS, 471, 987

Esteban, C., Méndez-Delgado, J. E., García-Rojas, J., et al. 2025, A&A, 697, A61
Filippenko, A. V. 1985, ApJ, 289, 475
Fukuda, N., & Hanawa, T. 2000, ApJ, 533, 911
Fukui, Y., Habe, A., Inoue, T., Enokiya, R., & Tachihara, K. 2021, PASJ, 73, S1
Gaia Collaboration 2020, VizieR Online Data Catalog: Gaia EDR3 (Gaia Collaboration, 2020), VizieR On-line Data Catalog: I/350 . Originally published in: 2021A&A...649A...1G; doi:10.5270/esa-1ug
Gallart, C., Bernard, E. J., Brook, C. B., et al. 2019, Nat. Astron., 3, 932
García-Benito, R., Díaz, A., Hägele, G. F., et al. 2010, MNRAS, 408, 2234
García-Rojas, J., Esteban, C., Peimbert, M., et al. 2006, MNRAS, 368, 253
Garner, III, R., Kennicutt, Jr, R. C., Drissen, L., et al. 2025, arXiv e-prints [arXiv:2510.03144]
Geen, S., Hennebelle, P., Tremblin, P., & Rosdahl, J. 2015, MNRAS, 454, 4484
Gonzalez-Delgado, R. M., Perez, E., Tenorio-Tagle, G., et al. 1994, ApJ, 437, 239
Greve, A. 2010, A&A, 518, A62
Gunasekera, C. M., van Hoof, P. A. M., Dehghanian, M., et al. 2025, arXiv e-prints [arXiv:2508.01102]
Hägele, G. F., Pérez-Montero, E., Díaz, Á. I., Terlevich, E., & Terlevich, R. 2006, MNRAS, 372, 293
Hawcroft, C., Leitherer, C., Aranguré, O., et al. 2025, ApJS, 280, 5
Herbst, T. M., Bizenberger, P., Blanc, G. A., et al. 2024, AJ, 168, 267
Herrera-Camus, R., Bolatto, A., Smith, J. D., et al. 2016, ApJ, 826, 175
Hester, J. J., Desch, S. J., Healy, K. R., & Leshin, L. A. 2004, Science, 304, 1116
Ivezić, Ž., Kahn, S. M., Tyson, J. A., et al. 2019, ApJ, 873, 111
Jin, Y., Sutherland, R., Kewley, L. J., & Nicholls, D. C. 2023, ApJ, 958, 179
Kalari, V. M. 2021, ApJ, 921, 81
Kennicutt, R. C., J. 1984, ApJ, 287, 116
Kennicutt, Robert C., J. 1998, ARA&A, 36, 189
Kewley, L. J., Nicholls, D. C., Sutherland, R., et al. 2019a, ApJ, 880, 16
Kewley, L. J., Nicholls, D. C., & Sutherland, R. S. 2019b, ARA&A, 57, 511
Khan, S., Rugel, M. R., Brunthaler, A., et al. 2024, A&A, 689, A81
Kollmeier, J., Anderson, S. F., Blanc, G. A., et al. 2019, BAAS, 51, 274
Kollmeier, J. A., Rix, H.-W., Aerts, C., et al. 2025, arXiv e-prints [arXiv:2507.06989]
Konidaris, N. P., Drory, N., Froning, C. S., et al. 2020, SPIE Conf. Ser., 11447, 1144718
Kreckel, K., Egorov, O. V., Egorova, E., et al. 2024, A&A, 689, A352
Kuhn, M. A., Hillenbrand, L. A., Feigelson, E. D., et al. 2022, ApJ, 937, 46
Kumari, N., James, B. L., & Irwin, M. J. 2017, MNRAS, 470, 4618
Liu, X. W., Barlow, M. J., Zhang, Y., Bastin, R. J., & Storey, P. J. 2006, MNRAS, 368, 1959
López-Hernández, J., Terlevich, E., Terlevich, R., et al. 2013, MNRAS, 430, 472
Luridiana, V., Morisset, C., & Shaw, R. A. 2015, A&A, 573, A42
Lynds, B. T., & Oneil, Earl J., J. 1986, AJ, 92, 1125
Maiolino, R., & Mannucci, F. 2019, A&A Rev., 27, 3
Malmann, J. A. H., Copetti, M. V. F., Dos Santos, I. C. F., Castañeda, J. M., & Vilchez, J. M. 2002, Revista Mexicana de Astronomia y Astrofisica Conference Series, 14, 57
Martig, M., Pinna, F., Falcón-Barroso, J., et al. 2021, MNRAS, 508, 2458
Martins, F., Schaerer, D., & Hillier, D. J. 2005, in SF2A-2005: Semaine de l'Astrophysique Francaise, eds. F. Casoli, T. Contini, J. M. Hameury, & L. Pagani, 633
Martins, F., Hervé, A., Bouret, J. C., et al. 2015, A&A, 575, A34
McLeod, A. F., Gritschneder, M., Dale, J. E., et al. 2016, MNRAS, 462, 3537
Méndez-Delgado, J. E., Amayo, A., Arellano-Córdova, K. Z., et al. 2022a, MNRAS, 510, 4436
Méndez-Delgado, J. E., Esteban, C., García-Rojas, J., & Henney, W. J. 2022b, MNRAS, 514, 744
Méndez-Delgado, J. E., Esteban, C., García-Rojas, J., et al. 2023a, MNRAS, 523, 2952
Méndez-Delgado, J. E., Esteban, C., García-Rojas, J., Kreckel, K., & Peimbert, M. 2023b, Nature, 618, 249
Méndez-Delgado, J. E., Skillman, E. D., Aver, E., et al. 2025, ApJ, 986, 74
Mesa-Delgado, A., Esteban, C., García-Rojas, J., et al. 2009, MNRAS, 395, 855
Mo, H., van den Bosch, F. C., & White, S. 2010, Galaxy Formation and Evolution (Cambridge: Cambridge University Press)
Morisset, C., Luridiana, V., García-Rojas, J., et al. 2020, Atoms, 8, 66
Nicholls, D. C., Sutherland, R. S., Dopita, M. A., Kewley, L. J., & Groves, B. A. 2017, MNRAS, 466, 4403
Nieva, M. F., & Przybilla, N. 2012, A&A, 539, A143
O'Dell, C. R., Ferland, G. J., Henney, W. J., et al. 2015, AJ, 150, 108
O'Dell, C. R., Ferland, G. J., & Peimbert, M. 2017, MNRAS, 464, 4835
Osterbrock, D. E. 1974, Astrophysics of Gaseous Nebulae (USA: University Science Books)
Osterbrock, D. E. 1989, Astrophysics of Gaseous Nebulae and Active Galactic Nuclei ((USA: University Science Books))
Osterbrock, D. E., & Ferland, G. J. 2006, Astrophysics of Gaseous Nebulae and Active Galactic Nuclei (USA: University Science Books)
Peimbert, M. 1967, ApJ, 150, 825
Peimbert, M., Sarmiento, A., & Fierro, J. 1991, PASP, 103, 815
Peimbert, M., Torres-Peimbert, S., & Luridiana, V. 1995, Revista Mexicana de Astronomia y Astrofisica Conference Series, 3, 296
Peimbert, M., Peimbert, A., Ruiz, M. T., & Esteban, C. 2004, ApJS, 150, 431
Peimbert, M., Peimbert, A., & Delgado-Inglada, G. 2017, PASP, 129, 082001
Peletier, R. F. 2013, in Secular Evolution of Galaxies, ed. J. Falcón-Barroso & J. H. Knapen (Cambridge, UK: Cambridge University Press), 353
Pérez-Montero, E. 2017, PASP, 129, 043001
Perruchot, S., Guy, J., Le Guillou, L., et al. 2018, SPIE Conf. Ser., 10702, 107027K
Puls, J., Urbaneja, M. A., Venero, R., et al. 2005, A&A, 435, 669
Ramachandran, V., Hamann, W. R., Oskinova, L. M., et al. 2019, A&A, 625, A104
Relaño, M., Monreal-Ibero, A., Vílchez, J. M., & Kennicutt, R. C. 2010, MNRAS, 402, 1635
Rho, J., Corcoran, M. F., Chu, Y.-H., & Reach, W. T. 2001, ApJ, 562, 446
Rho, J., Ramírez, S. V., Corcoran, M. F., Hamaguchi, K., & Lefloch, B. 2004, ApJ, 607, 904
Rho, J., Reach, W. T., Lefloch, B., & Fazio, G. G. 2006, ApJ, 643, 965
Rho, J., Lefloch, B., Reach, W. T., & Cernicharo, J. 2008, ASP Conf. Ser., 5, 509
Rodríguez, M. 1999, A&A, 351, 1075
Rodríguez, M., & Rubin, R. H. 2005, ApJ, 626, 900
Royer, M., Joncas, G., & Marquis, M. 2025, ApJ, 986, 159
Rubin, R. H., Simpson, J. P., Colgan, S. W. J., et al. 2016, MNRAS, 459, 1875
Sánchez, S. F., Cardiel, N., Verheijen, M. A. W., et al. 2007, A&A, 465, 207
Santolaya-Rey, A. E., Puls, J., & Herrero, A. 1997, A&A, 323, 488
Seaton, M. J. 1979, MNRAS, 187, 73
Simón-Díaz, S., & Stasińska, G. 2011, A&A, 526, A48
Simón-Díaz, S., Herrero, A., Esteban, C., & Najarro, F. 2006, A&A, 448, 351
Sota, A., Maíz Apellániz, J., Morrell, N. I., et al. 2014, ApJS, 211, 10
Stasińska, G., Morisset, C., Simón-Díaz, S., et al. 2013, A&A, 551, A82
Stickland, D. J., & Lloyd, C. 2001, The Observatory, 121, 1
Storey, P. J., & Hummer, D. G. 1995, MNRAS, 272, 41
Strömgren, B. 1939, ApJ, 89, 526
Tapia, M., Persi, P., Román-Zúñiga, C., et al. 2018, MNRAS, 475, 3029
Torii, K., Enokiya, R., Sano, H., et al. 2011, ApJ, 738, 46
Torii, K., Hattori, Y., Hasegawa, K., et al. 2017, ApJ, 835, 142
Worthey, G., Faber, S. M., & Gonzalez, J. J. 1992, ApJ, 398, 69
Yusef-Zadeh, F., Biretta, J., & Geballe, T. R. 2005, AJ, 130, 1171
Zhang, Y., Liu, X. W., Liu, Y., & Rubin, R. H. 2005, MNRAS, 358, 457

Appendix A: Integrated emission line fluxes

In Table A.1, we give all the observed $I(\lambda)$ and reddening corrected $F(\lambda)$ emission line fluxes for the fully integrated spectrum of M 20 as calculated in Sect. 3.3, together with the uncertainties. All fluxes are normalized to the Hβ = 100 with $I(\mathrm{H}\beta)$ = 1.60 × 10^{-9} erg/s/cm^2 and $F(\mathrm{H}\beta)$ = 1.16 × 10^{-8} erg/s/cm^2.

Table A.1: Fluxes for various emission lines of the fully integrated spectrum used in this work.

Line [Å]	Ion	$I(\lambda)$	$F(\lambda)$	Error [%]
3727	[O II]	96.012	135.443	1.2
3729	[O II]	129.775	183.008	0.9
3771	H I	1.599	2.236	37.2
3835	H I	3.21	4.43	15.1
4069	[S II]	1.964	2.544	16.7
4076	[S II]	0.439	0.567	55.5
4102	H I	19.694	25.249	1.6
4340	H I	38.871	46.11	1.0
4861	H I	100.0	100.0	0.1
5007	[O III]	47.456	45.401	0.5
5755	[N II]	1.272	0.996	22.4
6312	[S III]	1.294	0.887	14.1
6563	H I	397.338	256.899	5.7
6584	[N II]	145.697	93.746	16.3
6678	He I	3.892	2.451	0.8
6717	[S II]	49.362	30.802	0.3
6731	[S II]	36.813	22.897	0.3
7281	He I	0.833	0.457	26.6
7320	[O II]	3.203	1.741	9.8
7330	[O II]	2.658	1.442	12.0
9229	H I	5.328	1.958	2.3
9531	[S III]	109.6	38.347	1.2

Columns from left to right: Wavelength λ of the emission line in Å; Corresponding ion; Observed flux $I(\lambda)$; Reddening corrected flux $F(\lambda)$; Uncertainty of the reddening corrected flux in percent.

Appendix B: Modeling details for the Cloudy toy model of M 20

The photoionization model for M 20 is obtained using the latest version of CLOUDY (v25.00, see Gunasekera et al. 2025). A first sanity-check model is run without dust or filling factor, with a Black Body as ionizing source, at T_{eff} = 37500 K, with $Q_0 = 10^{49}$ s^{-1}, and a constant hydrogen density set to 100 cm^{-3} and an inner radius of 3 × 10^{17} cm (which leads to a rather filled sphere geometry). The model stops at a radius of 2.75 pc, the value obtained from the classical Strömgren radius definition from Eq. (3), using n_e = 106 cm^{-3} and T_e = 7115 K. The corresponding value for $L(\mathrm{H}\alpha)$ is 1.26 × 10^{37} erg/s, and $Q_0/L(\mathrm{H}\alpha)$ = 7.9 × 10^{11} erg^{-1}, close to the value of $Q_0/L(\mathrm{H}\alpha)$ = 7.32 × 10^{11} erg^{-1} derived in Eq. (7), the departure is mainly due to the way CLOUDY computes $L(\mathrm{H}\alpha)$.

When predicting the outer radius of a more complex nebula, several additional effects must be considered: dust can compete with neutral hydrogen (H^0) in absorbing ionizing photons, which reduces the size of the ionized region. Conversely, a filling factor smaller than 1.0 tends to increase the apparent size of the ionized region. Furthermore, the ratio $Q_0/L(\mathrm{H}\alpha)$ is also affected by the presence of dust.

A more complex model is therefore run, where the ionizing spectrum is taken from a FASTWIND model (Santolaya-Rey et al. 1997; Puls et al. 2005) extracted from the pyStarburst99 library (Hawcroft et al. 2025). An O-star at solar metallicity with T_{eff} = 37500 K is chosen. Its luminosity is defined by setting Q_0 = 1.8 × 10^{49} s^{-1} to reproduce the observed flux of Hα (see Sect. 3.4). The hydrogen density is set to decrease with the radius from 200 to 50 cm^{-3}. An inner radius of 3 × 10^{17} cm is set, to have the filled sphere expected from the spatial profile of the emission line shown in Fig. 4. A filling factor of 0.73 is used to let the outer radius reach a value of 3.06 pc, very close to the observed value (see Sect. 3.4). The abundance set is taken from Nicholls et al. (2017) based on log(O/H) = -3.36, with depletion. Grains are taken into account using the CLOUDY *grains ism* command. This model aims to reproduce the principal characteristics of the nebula, mainly its global emission of Hα and its size and temperature, but not trying to fine-tune the parameters to reproduce all the observables exactly. The model predicts $L(\mathrm{H}\alpha)$ = 8.7 × 10^{36} erg/s, close to the observed value (see Sect. 3.4). The mean temperature of H^+ is 8355 K, very consistent with the electron temperature reported in Table 1. The temperature is actually almost constant within the nebula, with an increase (800 K) in the very inner and outer regions.

The ratio between the rate of ionizing photons and the luminosity of the nebula is $Q_0/L(\mathrm{H}\alpha)$ = 2.1 × 10^{12} erg^{-1}. This value is greater than $Q_0/L(\mathrm{H}\alpha)$ = 7.32 × 10^{11} erg^{-1} obtained from Eq. (7), mainly due to the presence of dust in our model. The actual ratio may be slightly higher if the nebula is partially matter-bounded in some directions. This results from the [O I]λ6300 emission being unconstrained in our data, but the model predicts an intensity of 0.024 Hβ. However, the strong observed [S II] emission indicates that most regions of the nebula are close to the recombination front, implying that it is largely ionization-bounded overall.

A dust-free model is also computed with the same density law, chemical composition, and ionizing spectral energy distribution (SED). To fit the values of $L(\mathrm{H}\alpha)$ and the outer radius R, the stellar luminosity and filling factor must be tuned to Q_0 = 6.9 × 10^{48} s^{-1} and f_{fill} = 0.7. This illustrates the importance of dust in the absorption of ionizing SED (here, 60% of the ionizing SED is absorbed by dust) and in the relationship between $L(\mathrm{H}\alpha)$ and Q_0.

Our Cloudy toy model was designed to reproduce the observables directly relevant for estimating the ionizing photon rate, Q_0, namely the Hα luminosity, the electron temperature, and the Strömgren radius. Although metallicity and ionic abundances do influence the detailed excitation structure of the nebula, reasonable variations in chemical composition do not significantly change these predictions. The model does not aim to reproduce all line ratios because doing so would require a fully constrained ionizing SED, a detailed density structure, and assumptions about the dust content, which go beyond the scope of this work. However, the simplifications of our toy model do not affect our determination of Q_0 or the conclusions drawn from it.

Appendix C: Fitted temperature and abundance gradients

The temperature gradients obtained from the linear fits (see Sect. 4.2) are

$$\begin{aligned} T_e([O\,II])\,[K] &= (-77 \pm 49)\,[K/pc]\,(d \pm 0.7)\,[pc] \\ &\quad + (8212 \pm 63)\,[K], \end{aligned} \tag{C.1}$$

$$\begin{aligned} T_e([N\,II])\,[K] &= (-79 \pm 82)\,[K/pc]\,(d \pm 0.7)\,[pc] \\ &\quad + (8666 \pm 104)\,[K], \end{aligned} \tag{C.2}$$

$$\begin{aligned} T_e([S\,III])\,[K] &= (168 \pm 68)\,[K/pc]\,(d \pm 0.7)\,[pc] \\ &\quad + (8884 \pm 77)\,[K], \end{aligned} \tag{C.3}$$

$$\begin{aligned} T_e([S\,II])\,[K] &= (11 \pm 261)\,[K/pc]\,(d \pm 0.7)\,[pc] \\ &\quad + (10156 \pm 326)\,[K], \end{aligned} \tag{C.4}$$

where d is the radial distance to the central ionizing star HD 164492A. The corresponding oxygen abundance gradient derived from a linear fit (see Sect. 4.3) is

$$\begin{aligned} 12 + \log(O/H) &= (0.07 \pm 0.01)\,[dex/pc]\,(d \pm 0.7)\,[pc] \\ &\quad + (8.35 \pm 0.01). \end{aligned} \tag{C.5}$$

Appendix D: Uncertainties of resolved physical properties

In Figs. D.1 to D.4, we present the uncertainty maps for dust extinction (Fig. 3), electron densities (Fig. 5), electron temperatures (Fig. 7) and oxygen abundances (Fig. 9). The uncertainties for electron densities, electron temperatures, and oxygen abundances were derived from Monte Carlo Simulations as explained in detail in Sect. 3. While the uncertainty of the dust extinction was derived as the standard deviation of all calculated correction factors derived from the various hydrogen line ratios (see Sect. 3.1).

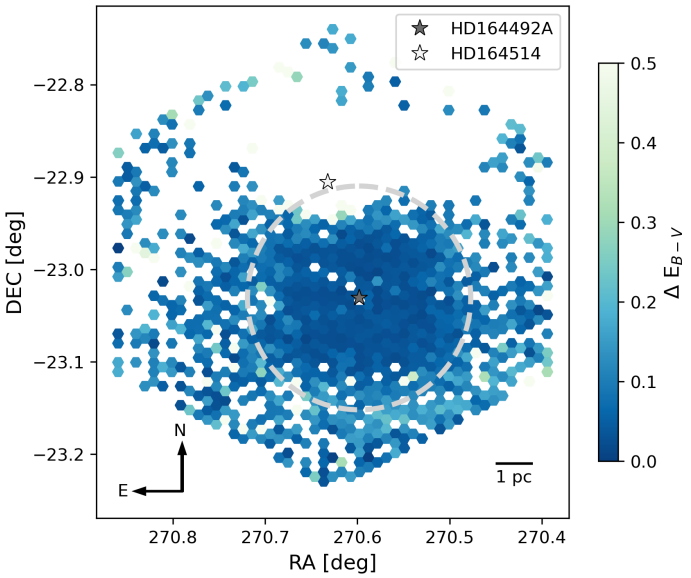

Fig. D.1: Uncertainties of the dust extinction map shown in Fig. 3. The position of HD 164492A is marked with a grey star. The extent of the measured Strömgren sphere (Sect. 3.4) is shown by a grey dashed circle.

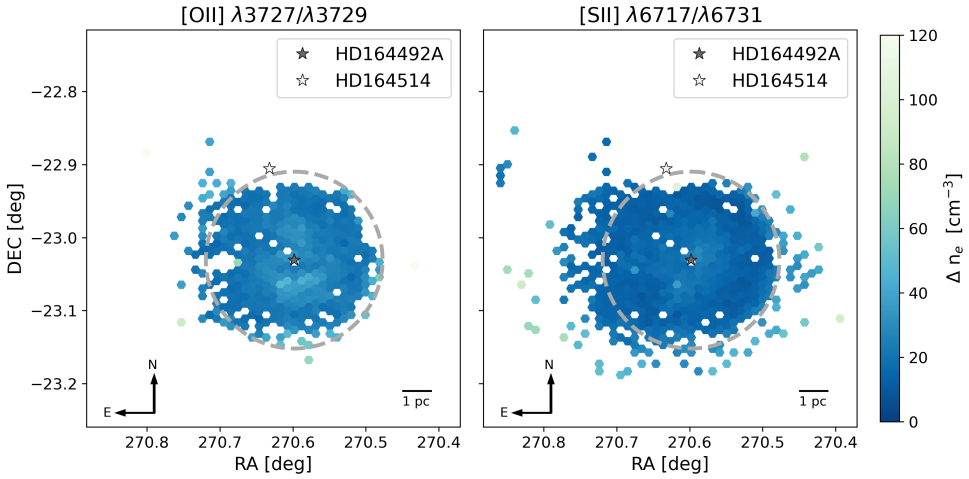

Fig. D.2: Uncertainties of the electron density maps shown in Fig. 5. The position of HD 164492A is marked with a grey star. The extent of the measured Strömgren sphere (Sect. 3.4) is shown by a grey dashed circle.

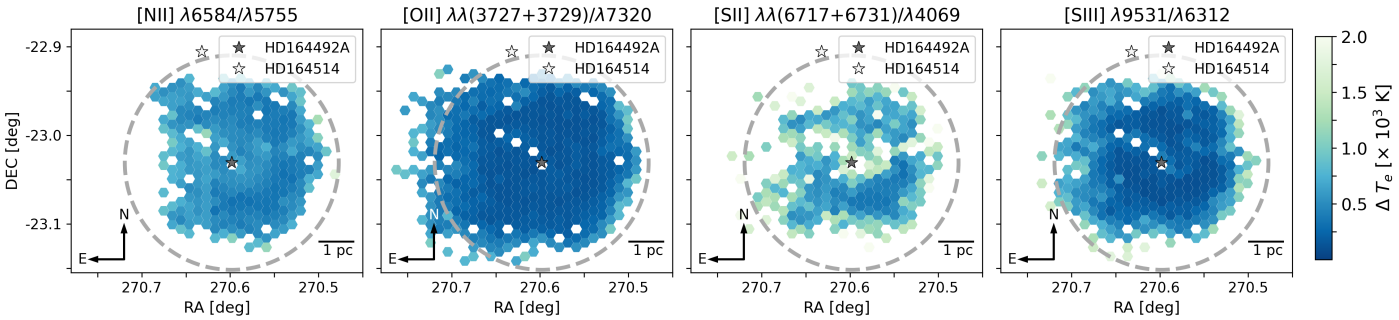

Fig. D.3: Uncertainties of the electron temperature maps shown in Fig. 7. The position of HD 164492A is marked with a grey star. The extent of the measured Strömgren sphere (Sect. 3.4) is shown by a grey dashed circle.

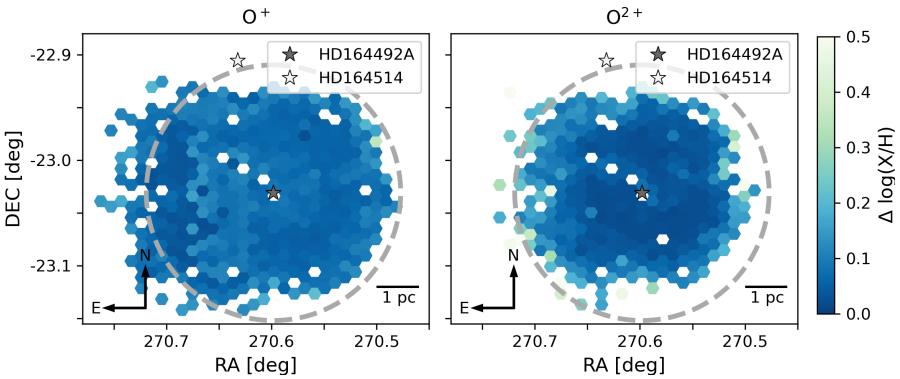

Fig. D.4: Uncertainties of the oxygen abundance maps shown in Fig. 9. The position of HD 164492A is marked with a grey star. The extent of the measured Strömgren sphere (Sect. 3.4) is shown by a grey dashed circle.